J. Fluid Mech. (1998), *vol.* 372, *pp.* 273–300. Printed in the United Kingdom

The stress singularity in surfactant-driven thin-film flows. Part 1. Viscous effects

By O. E. JENSEN[1] AND D. HALPERN[2]

[1]Department of Applied Mathematics and Theoretical Physics, University of Cambridge, Silver Street, Cambridge CB3 9EW, UK

[2]Department of Mathematics, University of Alabama, Tuscaloosa, AL 35487, USA

(Received 27 May 1997 and in revised form 14 April 1998)

The leading edge of a localized, insoluble surfactant monolayer, advancing under the action of surface-tension gradients over the free surface of a thin, viscous, fluid layer, behaves locally like a rigid plate. Since lubrication theory fails to capture the integrable stress singularity at the monolayer tip, so overestimating the monolayer length, we investigate the quasi-steady two-dimensional Stokes flow near the tip, assuming that surface tension or gravity keeps the free surface locally flat. Wiener–Hopf and matched-eigenfunction methods are used to compute the 'stick-slip' flow when the singularity is present; a boundary-element method is used to explore the nonlinear regularizing effects of weak 'contaminant' surfactant or surface diffusion. In the limit in which gravity strongly suppresses film deformations, a spreading monolayer drives an unsteady return flow (governed by a nonlinear diffusion equation) beneath most of the monolayer, and a series of weak vortices in the fluid ahead of the tip. As contaminant or surface diffusion increase in strength, they smooth the tip singularity over short lengthscales, eliminate the local stress maximum and ultimately destroy the vortices. The theory is readily extended to cases in which the film deforms freely over long lengthscales. Limitations of conventional thin-film approximations are discussed.

1. Introduction

The study of the spreading of surfactant monolayers on thin, viscous, horizontal fluid layers is motivated by numerous applications, ranging from respiratory mechanics (Grotberg 1994) to industrial coating and drying processes (e.g. O'Brien 1993; La Due, Muller & Swangler 1996). Spreading flows are driven by surface-tension gradients arising either from non-uniform concentration distributions of surfactant monolayers, or from the non-uniform thickness of an ultra-thin oil slick on an aqueous substrate. The majority of models are based upon lubrication theory, which yields coupled evolution equations for the surfactant distribution and the film thickness (Borgas & Grotberg 1988). These equations can incorporate a number of different effects that influence spreading rates and film deformation, including surface diffusion, surface viscosity, capillarity, surface contamination by a pre-existing surfactant species, van der Waals forces, surfactant solubility, gravity and inertia; recent reviews of the field are given by Jensen (1995) and Grotberg & Gaver (1996). Significant analytical progress has been possible because many unsteady spreading flows are asymptotically self-similar at large times (Jensen & Grotberg 1992; Espinosa *et al.* 1993; Jensen 1994).

Much of the interest in these flows focuses on the behaviour of the leading edge of a localized insoluble monolayer, which in the absence of surface diffusion behaves like an advancing rigid plate. Accordingly thin-film theory, incorporating Marangoni and viscous effects alone, predicts a discontinuity in shear stress and film height (Borgas & Grotberg 1988), representing a transition between an undisturbed film (of height H^*, say) and Couette flow beneath the advancing rigid monolayer, where the film locally has height $2H^*$. This shock-like structure may be smoothed over some lengthscale $\mathscr{X}^*$ by forces (such as gravity or capillarity) that smooth the fluid layer, leaving a jump in shear stress, or by those that smooth the surfactant distribution and thus also the fluid layer (such as surface diffusion or surface contamination). Some of the corresponding transition regions were investigated by Jensen & Grotberg (1992) in the limit $H^* \ll \mathscr{X}^* \ll L^*(t^*)$, where L^* is the monolayer length at time t^*: the assumption $\mathscr{X}^* \ll L^*(t^*)$ allowed the use of matched asymptotic expansions to compute quasi-steady 'inner' solutions in an otherwise unsteady analysis; the assumption $H^* \ll \mathscr{X}^*$ was required because these calculations represented short-wave limits of a long-wave (lubrication) theory. Local Stokes-flow solutions for the transition regions associated with surface diffusion or contaminant in the limit $\mathscr{X}^* \ll H^*$ (regarding the fluid layer as infinitely deep) have been determined by Harper (1992).

Despite its success and widespread use, lubrication theory is unable to describe a fundamental feature of surfactant-spreading flows, namely that at the advancing tip of a localized, non-diffusing monolayer there is an integrable ($r^{-1/2}$) singularity in shear stress, pressure and vorticity; here r is the distance from the singularity (Carrier & Lin 1948; Harper 1992). The primary objective of this study is to remedy this deficiency in existing thin-film models, by considering in detail the region of asymptotic non-uniformity at the monolayer's leading edge. We shall show that, in general, this requires consideration of a local two-dimensional, quasi-steady Navier–Stokes flow. Fortunately, in many practical circumstances, restoring forces such as gravity and surface tension are sufficiently strong to act over lengthscales much longer than H^*, ensuring that the free surface is locally horizontal, even though there may be substantial film deformation elsewhere. Indeed, even in the absence of restoring forces, on the shortest lengthscales near the singularity the free surface *must* be locally planar (i.e. have continuous slope, Michael 1958; Tayler 1973), although in principle it is possible for the free surface to have a coincident integrable singularity in curvature (Schultz & Gervasio 1990). Since a monolayer typically slows as it spreads, inertial effects may be significant near the leading edge during the early stages of spreading (Jensen 1995), whereas viscous effects dominate at later times. In the present paper we use a Stokes-flow approximation to describe the later-time flow; in the second part of this study (Jensen 1998), high-Reynolds-number asymptotics are used to describe key features of the flow near the monolayer tip at earlier times.

When the monolayer-tip singularity is present, the local Stokes flow has similarities with the 'stick-slip' die-swell problem of a viscous jet leaving a nozzle (Richardson 1970; Trogdon & Joseph 1980, 1981; see also Salamon *et al.* 1995 and references therein), with certain crack-propagation problems in linearly elastic media (e.g. Foote & Buchwald 1985), with the thermocapillary-driven flow beneath a stationary monolayer (Carpenter & Homsy 1985), with entry flows beneath plane slider bearings (e.g. Malvano & Vatta 1998) and (as we shall show) it is identical to the problem of viscous flow past a semi-infinite plate moving steadily down the centre of a channel. Solutions of the latter problem, which is linear but with mixed boundary conditions, can be obtained by the Wiener–Hopf technique (Graebel 1965; his solution was later corrected by Porter & Dore 1974 and others, e.g. Kim & Chung 1984; Davis &

Abrahams 1996). To demonstrate some of the more striking features of this flow, we have recomputed the solution (in § 3 below) with the numerically more efficient method of matched biorthogonal eigenfunction expansions (e.g. Trogdon & Joseph 1980, 1981; Schultz & Gervasio 1990), using the Wiener–Hopf method to identify details such as the strength of the singularity. We show for example that, in the limit in which the gravitational restoring force is very strong, the advancing monolayer drives ahead of itself a series of weak recirculating vortices (of the type described by Moffatt 1964), the intensity of which decays rapidly over an $O(H^*)$ distance from the monolayer tip. For a monolayer of length $L^*(t^*) \gg H^*$, the effect of the singularity is felt over horizontal lengthscales $\mathscr{X}^* = O(H^*)$, yielding an $O(H^*)$ viscous correction to the monolayer length (given in equation (6.2) below).

A useful comparison can be drawn between the advancing tip of a localized monolayer and the motion of an advancing contact line of a fluid over an otherwise dry solid surface, at which a non-integrable stress singularity arises if a no-slip boundary condition is imposed (Dussan V. 1979). The singularity in the latter case is typically relieved either by imposing an *ad hoc* slip condition or by allowing for the existence of an ultra-thin precursor film. Although the weaker singularity in the surfactant-spreading problem allows a self-consistent flow to be computed, this singularity too is readily eliminated by weak perturbations. Either weak surface contamination (by pre-existing surfactant) ahead of the monolayer or weak surface diffusion smooths the tip singularity over some lengthscale $\mathscr{X}^*$, but thereby renders the local Stokes-flow problem nonlinear. We therefore use a boundary-element method (BEM) to link the asymptotic results of Harper (1992) (for weak contaminant, with $\mathscr{X}^* \ll H^*$) and lubrication theory (for stronger contaminant, with $\mathscr{X}^* \gg H^*$). It is shown for example that the vortices ahead of the monolayer vanish abruptly once the level of contaminant exceeds a critical value. Weak surface diffusion is shown to act in a similar manner.

At present, there is limited experimental confirmation of many of the existing theoretical predictions of surfactant-spreading flows. Experiments are hampered by the difficulty of depositing a monolayer on a thin film without introducing unwanted flow disturbances, which may induce film rupture, for example (Kheshgi & Scriven 1991; Gaver & Grotberg 1992). Further, for all but ultra-thin layers, gravitational effects dominate relatively early during the spreading process, suppressing film disturbances, generating a reverse flow near the lower boundary (Pimputkar & Ostrach 1980; Gaver & Grotberg 1990, 1992) and ultimately returning the free surface to the horizontal. A further aim of the present study is therefore to extend existing models to the practically significant regime in which the fluid layer is almost flat along its entire length. In this limit, a single nonlinear diffusion equation ((2.9*a*), below) governs most of the surfactant distribution; (2.9*a*) has similarity solutions sharing scalings similar to the coupled evolution equations arising when the surface deforms freely (Jensen & Grotberg 1992), so that a planar monolayer strip again spreads with $L^*(t^*) \propto t^{*1/3}$ to leading order, for example. Away from the leading edge, spreading is driven predominantly by an unsteady 'return flow,' familiar from studies of thermocapillary flows in long slots (e.g. Sen & Davis 1982): the flow is nearly horizontal, with a forward stress-driven component near the free surface, and a backward pressure-driven component beneath. The return flow streamlines cannot be 'closed' beneath the tip of a localized monolayer without consideration of short-lengthscale effects, however.

The model is outlined in § 2, where it is shown how a restricted class of Navier–Stokes flows in a rectangular domain constitute formal 'inner' problems for a large family of surfactant-spreading flows. We discuss the stick-slip Stokes-flow problem

in § 3, and the corresponding effects of weak contaminant and surface diffusion are treated in § 4 and § 5. Inertial effects, and their interaction with those of contaminant, are explored in Part 2 (Jensen 1998). The main conclusions of this study are summarized in § 6.

2. The model

Consider a stationary fluid layer of density ρ^*, viscosity μ^* and initially uniform thickness H^* lying on a flat, horizontal, impermeable plane, in the presence of a vertical gravitational field g^*. An insoluble surfactant monolayer is deposited on the free surface over some lengthscale substantially larger than H^*, with an initial concentration of typical magnitude Γ_0^*. A 'contaminant' monolayer may be present elsewhere on the free surface, having weak, uniform concentration $\gamma\Gamma_0^*$, where $0 \leqslant \gamma \ll 1$. The surface tension of the surfactant-covered interface is assumed to be a linearly decreasing function of monolayer concentration, so that $\sigma^* = \sigma_0^* - A\Gamma^* \equiv S^*(\mathscr{S} - \Gamma)$; here Γ^* is the surfactant concentration and $\Gamma = \Gamma^*/\Gamma_0^*$ is its non-dimensional equivalent. The surfactant activity $A^* = -\mathrm{d}\sigma^*/\mathrm{d}\Gamma^*$ is assumed to be a positive constant, an approximation that is valid for dilute gaseous monolayers. The spreading coefficient $S^* = A^*\Gamma_0^*$ represents the scale of surface tension reduction by the monolayer; it is this surface-tension difference, distributed along the length of the deposited monolayer, that drives a spreading flow. It is offset by $S_\infty^* = \gamma A^*\Gamma_0^*$, the surface-tension reduction due to the weak contaminant. The surface tension of the interface when clean, σ_0^*, is represented by the dimensionless parameter $\mathscr{S} = \sigma_0^*/S^* > 1$.

We define a velocity scale $U^* = S^*/\mu^*$, a length scale H^*, a time scale $T^* = H^*/U^*$ and a pressure scale μ^*U^*/H^*. Gravity is represented through a parameter (a form of Bond number) $\mathscr{G} = \rho^* g^* H^{*2}/S^*$. For a typical terrestrial experiment with a 1 mm layer of water, $\rho^* \approx 1\ \mathrm{g\,cm^{-3}}$, $g^* \approx 10^3\ \mathrm{cm\,s^{-2}}$, $S^* \approx 10\ \mathrm{g\,s^{-2}}$, $H^* \approx 0.1$ cm and $\mu^* \approx 10^{-2}\ \mathrm{g\,cm^{-1}\,s^{-1}}$, so that $\mathscr{G} \approx 1$. Thus $\mathscr{G}$ is appreciable for all but ultra-thin films. Surface diffusion of the surfactant is represented by $\mathscr{D} = D^*/(U^*H^*)$, where D^* is a surface diffusivity, assumed constant; since $D^* \leqslant 10^{-5}\ \mathrm{cm^2\,s^{-1}}$ for typical surfactants (Agrawal & Neuman 1988), $\mathscr{D} \leqslant 10^{-7}$ in a standard experiment, so the effects of contaminant, represented by γ, will generally be stronger. The Reynolds number of the flow, $\mathscr{R} = \rho^* H^* S^*/\mu^{*2}$, is 10^4 for the parameter values given above; for the present we allow $\mathscr{R}$ to remain moderately large in a sense to be defined below.

Using the scales given above, we consider two-dimensional planar flows by introducing Cartesian coordinates (x, y) and a velocity field $\boldsymbol{u} = (u, v)$, with the fluid layer lying between the rigid plane at $y = 0$ and a free surface at $y = h(x, t)$; the undisturbed layer has $h = 1$. The flow is governed by the non-dimensional Navier–Stokes equations,

$$\nabla \cdot \boldsymbol{u} = 0, \quad \mathscr{R}\,[\boldsymbol{u}_t + (\boldsymbol{u} \cdot \nabla)\boldsymbol{u}] = -\nabla p + \nabla^2 \boldsymbol{u} - \mathscr{G}\hat{\boldsymbol{y}}, \tag{2.1a,b}$$

where p is the fluid pressure and $\hat{\boldsymbol{y}}$ is the unit vector in the y-direction; at the planar boundary $\boldsymbol{u}(x, 0) = \boldsymbol{0}$. Above the fluid is an inviscid gas at zero pressure, so the free-surface stress and kinematic boundary conditions at $y = h(x, t)$ are

$$\boldsymbol{n} \cdot \boldsymbol{T} \cdot \boldsymbol{n} = (\mathscr{S} - \Gamma)\kappa, \quad \boldsymbol{t} \cdot \boldsymbol{T} \cdot \boldsymbol{n} = -\nabla_s \Gamma, \quad h_t + uh_x = v. \tag{2.2a–c}$$

Here $\boldsymbol{n} \equiv (-h_x, 1)/\Delta$ and $\boldsymbol{t} \equiv (1, h_x)/\Delta$, where $\Delta \equiv (1 + h_x^2)^{1/2}$, are the unit normal and tangent vectors to the free surface respectively; the interfacial curvature is $\kappa = -\nabla_s \cdot \boldsymbol{n} = h_{xx}/\Delta^3$, where $\nabla_s \equiv (\boldsymbol{I} - \boldsymbol{nn}) \cdot \nabla$ is the surface gradient operator. The

stress tensor is $\boldsymbol{T} = -p\boldsymbol{I} + \nabla\boldsymbol{u} + \nabla\boldsymbol{u}^T$. The normal and tangential stress conditions (2.2*a*, *b*) at $y = h(x,t)$ may then be written

$$-p + \frac{2}{\Delta^2}\left[(h_x^2 - 1)u_x - h_x\left(u_y + v_x\right)\right] = (\mathscr{S} - \Gamma)\frac{h_{xx}}{\Delta^3}, \tag{2.3}$$

$$(1 - h_x^2)(u_y + v_x) - 2h_x(u_x - v_y) = -\Delta\Gamma_x. \tag{2.4}$$

Writing $\boldsymbol{u}_s = (u_s, v_s) = (\boldsymbol{I} - \boldsymbol{nn})\cdot\boldsymbol{u}$, the surfactant transport equation is

$$\Gamma_t + \nabla_s\cdot(\boldsymbol{u}_s\Gamma) + (\nabla_s\cdot\boldsymbol{n})(\boldsymbol{n}\cdot\boldsymbol{u})\,\Gamma = \mathscr{D}\nabla_s^2\Gamma. \tag{2.5}$$

We consider flows that satisfy $h \to 1$, $\Gamma \to \gamma$ as $x \to \infty$; a range of upstream conditions at $x = 0$ are allowable.

The standard lubrication-theory approximation of (2.1)–(2.5) is briefly reviewed in § 2.1 below. We then consider two distinct limits: that in which $\mathscr{G} \gg 1$ (§ 2.2), so that the film is almost flat over the length of the monolayer; and that in which restoring forces are relatively weak ($\mathscr{G} = 0$, Appendix A), so that the film deforms significantly over lengthscales long compared to the film depth but short compared to the length of the monolayer. The latter limit was considered by Jensen & Grotberg (1992); the former 'flat-film' limit, although somewhat simpler, has previously been largely overlooked. In each case, we show how the presence or near-presence of a stress singularity at the monolayer's leading edge, which arises in the limit $\gamma \to 0$, $\mathscr{D} \to 0$, implies that the local flow is governed, in general, by a family of steady Navier–Stokes problems, defined in a long, rectangular domain, parameterized by the local film height. Late in spreading, when viscous effects dominate inertia, a rescaling given in § 2.3 shows that only a single canonical Stokes-flow problem need be considered, parameterized by γ and $\mathscr{D}$. Solutions to this Stokes-flow problem are given in §§ 3–5 below; the Navier–Stokes problem for a 'flat' film is examined using boundary-layer theory in Part 2 (Jensen 1998).

2.1. *Thin-film approximations for long, spreading monolayers*

Thin-film approximations of (2.1)–(2.5) have been derived in detail elsewhere (e.g. Borgas & Grotberg 1988; Gaver & Grotberg 1990; Jensen & Grotberg 1992), so here we simply present the resulting evolution equations. Let $\bar{X} = \epsilon x$ represent a long length, corresponding to the length of the spreading monolayer, and $T = \epsilon^2 t$ a slow time, where $0 < \epsilon \ll 1$. We suppose that $\mathscr{G}$ and $\mathscr{S}$ are $O(1)$, that $\mathscr{R} = o(1/\epsilon^2)$, and that $\mathscr{D}$ and γ are $O(\epsilon)$. To leading order in ϵ, the pressure in the fluid is hydrostatic, so that $p = \mathscr{G}(h - y)$, and viscous stresses (represented by u_{yy}) balance horizontal pressure gradients and surface (Marangoni) stresses. The flow at leading order is then governed by the coupled evolution equations

$$h_T + Q_{\bar{X}} = 0, \qquad Q = -\tfrac{1}{3}\mathscr{G}h^3h_{\bar{X}} - \tfrac{1}{2}h^2\Gamma_{\bar{X}}, \tag{2.6a}$$

$$\Gamma_T + q_{\bar{X}} = 0, \qquad q = -\tfrac{1}{2}\mathscr{G}\Gamma h^2h_{\bar{X}} - h\Gamma\Gamma_{\bar{X}}. \tag{2.6b}$$

The streamfunction for this flow in the frame of the wall is $\psi = \frac{1}{6}\mathscr{G}h_{\bar{X}}y^2(y - 3h) - \frac{1}{2}\Gamma_{\bar{X}}y^2$, and the corresponding velocity field is $\boldsymbol{u} = (\epsilon\psi_y, -\epsilon^2\psi_{\bar{X}})$. Capillary forces and surface diffusion, of $O(\epsilon^2\mathscr{S})$ and $O(\mathscr{D})$ respectively, do not arise at leading order in this approximation, although they were retained in composite expansions used in earlier models (Gaver & Grotberg 1990; Jensen & Grotberg 1992). Likewise, the downstream boundary condition becomes $h \to 1$, $\Gamma \to 0$ as $\bar{X} \to \infty$, since weak contaminant is negligible at this order. The leading edge of the monolayer, within the resolution of the long lengthscale, is at $\bar{X} = L(T)$, say, so that $\Gamma = 0$ for $\bar{X} \geqslant L(T)$.

As $\bar{X} \to L(T)\pm$ with $\mathscr{G} = O(1)$, continuity of the fluxes Q and q demands that there be jumps in gradient of h and Γ across $\bar{X} = L(T)$ given by

$$\tfrac{1}{12}\mathscr{G}h^3 h_{\bar{X}}^- - \tfrac{1}{2}hL_T = \tfrac{1}{3}\mathscr{G}h^3 h_{\bar{X}}^+, \quad h\Gamma_{\bar{X}}^- + L_T + \tfrac{1}{2}\mathscr{G}h^2 h_{\bar{X}}^- = 0 \qquad (2.7a,b)$$

where $h_{\bar{X}}^+$ ($h_{\bar{X}}^-$) is the limiting value of $h_{\bar{X}}$ as $\bar{X} \to L$ with $\bar{X} > L$ ($\bar{X} < L$). Since a spreading monolayer slows as it spreads, the hydrostatic restoring force (represented by the terms proportional to $\mathscr{G}$ in (2.6)) becomes increasingly powerful and film deformations are ultimately suppressed, so that $h(L, T)$ approaches 2 at early times, falling to 1 at late times (Gaver & Grotberg 1990). Meanwhile, a gravity-driven disturbance to the film propagates ahead of the slowly advancing monolayer tip, and a region of reversed flow develops along $y = 0$ beneath the monolayer. The limits $T \gg 1$ and $T \ll 1$ in (2.6) with $\mathscr{G} = O(1)$ are therefore well represented respectively by the limits $\mathscr{G} \gg 1$ and $\mathscr{G} \ll 1$ with $T = O(1)$. We consider these two limits in more detail in § 2.2 and Appendix A respectively; § 2.3 below applies also to the case $\mathscr{G} = O(1)$ with $T = O(1)$.

2.2. *Strong restoring forces: the flat-film limit*

Assuming $\mathscr{G} \gg 1$, we pose an expansion that is valid for the region beneath the monolayer, $(h, \Gamma) = (1, \Gamma_0) + \mathscr{G}^{-1}(h_1, \Gamma_1) + o(\mathscr{G}^{-1})$, with $(Q, q) = (Q_0, q_0) + o(1)$. At leading order (2.6) yields $Q_0 = -\frac{1}{3}h_{1\bar{X}} - \frac{1}{2}\Gamma_{0\bar{X}}$ and $q_0 = -\frac{1}{2}\Gamma_0 h_{1\bar{X}} - \Gamma_0\Gamma_{0\bar{X}}$. Since $h_T = O(\mathscr{G}^{-1})$, we must have $Q_{0\bar{X}} = 0$, so if $Q_0 = 0$ at $\bar{X} = 0$, then $Q_0 = 0$ everywhere beneath the monolayer, representing a balance between forward surface-driven flow and gravitationally-driven reverse flow. Thus

$$h_1 = \mathscr{H}(T) - \tfrac{3}{2}\Gamma_0, \quad q_0 = -\tfrac{1}{4}\Gamma_0\Gamma_{0\bar{X}} \qquad (2.8a,b)$$

where $\mathscr{H}(T)$ can be determined by considering the flow disturbance ahead of the monolayer; in Appendix B we show that for a monolayer of fixed mass (i.e. fixed total concentration) $\mathscr{H} = O((\mathscr{G}T)^{-1/2})$, so in this particular case $\mathscr{H}$ does not strictly appear in (2.8*a*) at this order, although we retain it below for completeness. Further, it follows that

$$\Gamma_{0T} = \tfrac{1}{4}(\Gamma_0\Gamma_{0\bar{X}})_{\bar{X}}, \quad \psi(\bar{X}, y) \sim -\tfrac{1}{4}\Gamma_{0\bar{X}}(y^3 - y^2). \qquad (2.9a,b)$$

The surfactant distribution is therefore governed by a single nonlinear diffusion equation (2.9*a*), the late-time analogue of (2.6); a model equation of this form was proposed by Jensen (1995) and an analogous equation for non-diffusing soluble surfactant was given by Thess, Spirn & Jüttner (1997). The linearized form of (2.9*a*), in which Γ_0 varies weakly around a uniform mean value, was obtained by Dimitrov *et al.* (1978). The leading-order streamfunction (2.9*b*) has the simple form of a return flow.

For a smooth, monotonically decreasing surfactant distribution, with $\Gamma_0 \gg \epsilon$ everywhere, the resulting spreading flow may be described uniformly by (2.9); the flow has closed streamlines, with forward motion in the upper third of the fluid layer and a reverse flow beneath it, as illustrated for a typical Γ_0-distribution in figure 1. Where the free surface is being stretched ($\Gamma_{0\bar{X}\bar{X}} < 0$), fluid is drawn upwards towards the free surface; where the surface is being compressed, there is downward displacement of fluid. The free surface rises gently along the length of the flow region (see (2.8*a*)), providing a hydrostatic pressure gradient to drive the reverse flow. This picture may become asymptotically non-uniform if $\Gamma_0 = O(\epsilon)$ anywhere, however, since then the flow may vary over lengthscales that are too short for lubrication theory to remain valid.

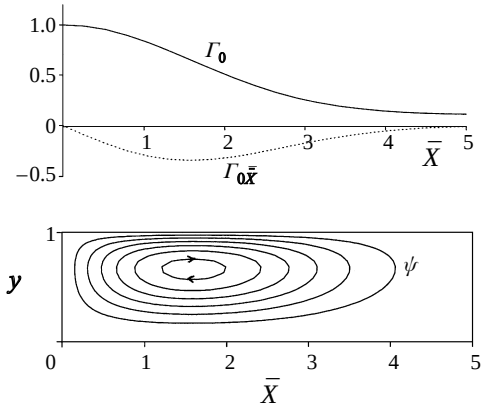

FIGURE 1. A spreading monolayer on a flat film, for which $\Gamma_0 \gg \epsilon$ everywhere, showing the return-flow streamfunction (2.9*b*) for a typical concentration distribution Γ_0. The surface velocity is $-\frac{1}{4}\Gamma_{0\bar{X}}$.

Such a difficulty arises for a localized monolayer spreading over a clean interface. In this important limit, similarity solutions of (2.9*a*) can be constructed. A spreading monolayer strip, for example, for which $\int_0^L \Gamma_0 \, \mathrm{d}\bar{X} = M =$ constant and $\Gamma_0 = 0$ in $\bar{X} > L(T)$, is given by the well-known Pattle–Barenblatt solution (e.g. Pattle 1959)

$$\Gamma_0(\bar{X}, T) = \frac{2}{3T}\left(L^2 - \bar{X}^2\right), \quad 0 \leqslant \bar{X} < L(T) = \left(\tfrac{9}{4}MT\right)^{1/3}. \qquad (2.10a,b)$$

Like the analogous fixed-mass solution with $\mathscr{G} = 0$ (the spreading-strip solution in Jensen & Grotberg 1992), this monolayer spreads like $T^{1/3}$, although it is $(9/48)^{1/3} \approx 57\%$ of the length it has when the film can deform freely, because steeper surface-tension gradients are required to drive the reverse flow.

The exact solution (2.10) illustrates how, at the leading edge of an advancing localized monolayer, lubrication theory predicts the existence of an abrupt jump in shear stress (i.e. in $-\Gamma_{0\bar{X}}$). More generally, if the leading edge lies at $\bar{X} = L(T)$, so that the monolayer tip advances at a slow speed (in (x,t)-variables) $V = \epsilon L_T$, the local solution of (2.9*a*) is

$$\Gamma_0 \sim \begin{cases} -4L_T(\bar{X} - L) \equiv -4V\left[x - (L/\epsilon)\right] & \text{for } \bar{X} \to L(T), \\ 0 & \text{for } \bar{X} > L(T). \end{cases} \qquad (2.11)$$

This thin-film approximation therefore fails to capture a smooth transition at $\bar{X} = L(T)$ between the return flow beneath the monolayer (2.9*b*) and the undisturbed film ahead of it; the local Navier–Stokes problem must instead be considered (see § 2.2.1 below). Before doing so, however, we note that if $\epsilon \ll \gamma \ll 1$, the downstream boundary condition $\Gamma \to 0$ as $\bar{X} \to \infty$ (given after (2.6)) may be replaced by $\Gamma \to \gamma$, and then the jump in shear stress implicit in (2.11) can be smoothed by contaminant over a long x-lengthscale γ/V: setting $\Gamma_0 = \gamma G(\zeta)$, $\bar{X} = L(T) + \gamma\zeta/L_T$, (2.9*a*) reduces at leading order to $-G_\zeta = \frac{1}{4}(GG_\zeta)_\zeta$ which, with $G \to 1$ as $\zeta \to \infty$, implies that $G_\zeta = 4[(1/G) - 1]$, so that

$$G + \log(G - 1) = 4(\zeta_0 - \zeta), \quad \psi \sim -\tfrac{1}{4}L_T G_\zeta(y^3 - y^2) \qquad (2.12a,b)$$

for some ζ_0 (see figure 2). As $|\zeta| \to \infty$, (2.12) matches with (2.11) at leading order for $\gamma \ll 1$. This 'inner' solution is the flat-film analogue of the contaminant transition

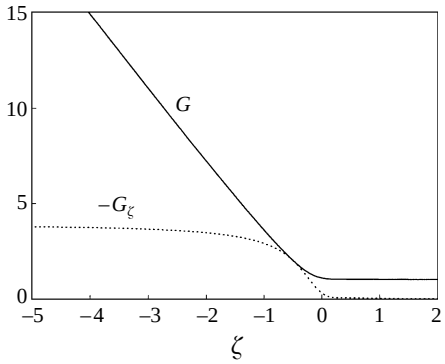

FIGURE 2. The lubrication-theory solution (2.12*a*) with $\zeta_0 = 0$ for a contaminant transition region on a flat film, which may smooth the jump in shear stress described in (2.11); the shear stress $-G_\zeta$ is proportional to the surface velocity; $-G$ is proportional to the pressure in the fluid layer and the displacement of the nearly-flat free surface.

region for a deforming interface given in Jensen & Grotberg (1992). Since (2.12) is based on lubrication theory, however, it becomes invalid once $\gamma = O(\epsilon)$; the generalization of this solution to smaller values of γ is given in §4 below.

2.2.1. *The Navier–Stokes flow at the tip of a monolayer on a flat film*

To explore the transition (2.11), we move to the frame of the monolayer's leading edge by setting $x = (L/\epsilon) + \tilde{x}$ and seek quasi-steady solutions as $\epsilon \to 0$, noting that this frame moves slowly with speed $V = O(\epsilon)$. The inner limit of the outer solution (2.11) has

$$\Gamma(\tilde{x}) \sim \begin{cases} -4V\tilde{x} \\ 0, \end{cases} \qquad p(\tilde{x}, y) \sim \begin{cases} \mathscr{G}(1-y) + \mathscr{H} + 6V\tilde{x}, & \tilde{x} \to -\infty \\ \mathscr{G}(1-y) + \mathscr{H}, & \tilde{x} \to \infty, \end{cases} \tag{2.13}$$

with $h \sim 1 + p(\tilde{x}, 1)/\mathscr{G}$. We rescale (2.1)–(2.5), setting $p(x, y, t) = \mathscr{G}(1-y) + \mathscr{H} + V\tilde{p}(\tilde{x}, y)$, $\boldsymbol{u}(x, y, t) = V\tilde{\boldsymbol{u}}(\tilde{x}, y)$, $\Gamma(x, t) = V\tilde{\Gamma}(\tilde{x})$, and set

$$\tilde{\mathscr{R}} = \mathscr{R}V = o(1/\epsilon), \quad \tilde{\gamma} = \gamma/V = O(1), \quad \tilde{\mathscr{D}} = \mathscr{D}/V = O(1). \tag{2.14a–c}$$

We then expand in powers of $1/\mathscr{G} \ll 1$, using $(\tilde{p}, \tilde{\boldsymbol{u}}, \tilde{\Gamma}) = (\tilde{p}_0, \tilde{\boldsymbol{u}}_0, \tilde{\Gamma}_0) + o(1)$ and expressing the boundary location as $h = 1 + [\mathscr{H} + V\tilde{h}_1(\tilde{x})]/\mathscr{G} + o(\mathscr{G}^{-1})$, which yields the following Navier–Stokes problem defined in $-\infty < \tilde{x} < \infty$, $0 \leqslant y \leqslant 1$:

$$\tilde{\nabla} \cdot \tilde{\boldsymbol{u}}_0 = 0, \quad \tilde{\mathscr{R}}\left[-\tilde{\boldsymbol{u}}_{0\tilde{x}} + (\tilde{\boldsymbol{u}}_0 \cdot \tilde{\nabla})\tilde{\boldsymbol{u}}_0\right] = -\tilde{\nabla}\tilde{p}_0 + \tilde{\nabla}^2\tilde{\boldsymbol{u}}_0, \quad \tilde{\boldsymbol{u}}_0(\tilde{x}, 0) = \boldsymbol{0}. \tag{2.15a–c}$$

Here $\tilde{\nabla} \equiv (\partial/\partial\tilde{x}, \partial/\partial y)$. The free-surface boundary conditions, with the dependent variables Taylor-expanded about $y = 1$, are

$$\tilde{v}_0 = 0, \quad \tilde{u}_{0y} = -\tilde{\Gamma}_{0\tilde{x}}, \quad -\tilde{\Gamma}_{0\tilde{x}} + (\tilde{u}_0\tilde{\Gamma}_0)_{\tilde{x}} = \tilde{\mathscr{D}}\tilde{\Gamma}_{0\tilde{x}\tilde{x}}. \tag{2.16a–c}$$

Integrating (2.16*c*), assuming $\tilde{\Gamma}_0 \to \tilde{\gamma}$ as $\tilde{x} \to \infty$, and applying the normal stress condition (2.3), we have on $y = 1$

$$\tilde{\Gamma}_0(1 - \tilde{u}_0) + \tilde{\mathscr{D}}\tilde{\Gamma}_{0\tilde{x}} = \tilde{\gamma}, \quad \tilde{h}_1 = \tilde{p}_0 + 2\tilde{u}_{0\tilde{x}}. \tag{2.17a,b}$$

With $\mathscr{S} = O(1)$, the capillary term in the normal stress condition is $O(\mathscr{S}/\mathscr{G})$ and so it is negligible. In the far field the flow must match on to the external lubrication

theory solution (2.13). With $\tilde{\boldsymbol{u}}_0 = (\tilde{\psi}_y, -\tilde{\psi}_{\tilde{x}})$, we require

$$\tilde{\Gamma}_0 \sim \begin{cases} -4\tilde{x} \\ \tilde{\gamma}, \end{cases} \qquad \tilde{p}_0 \sim \begin{cases} 6\tilde{x} \\ 0, \end{cases} \quad \tilde{\psi} \sim \begin{cases} (y^3 - y^2) & \text{for } \tilde{x} \to -\infty, \\ 0 & \text{for } \tilde{x} \to \infty. \end{cases} \tag{2.18a–c}$$

Equations (2.15)–(2.18) will be solved for $\tilde{\mathscr{R}} \ll 1$ in § 3–§ 5 below and for $1 \ll \tilde{\mathscr{R}} \ll 1/\epsilon$ in Part 2 (Jensen 1998).

2.3. *The canonical Stokes flow at the leading edge of a monolayer*

When the film is constrained to be almost flat everywhere under strong gravity (§ 2.2), and when it can deform freely under surface tension alone (Appendix A), a local analysis of the flow near the monolayer tip yields two different 'inner' Navier–Stokes problems (see (2.15)–(2.18) and Appendix A respectively). In the limit $\tilde{\mathscr{R}} \to 0$, we show here that these reduce to a single Stokes flow, which also describes a much wider class of problems, including the cases when $\mathscr{G} = O(1)$ with $T = O(1)$ in (2.6), when gravity has a component in the x-direction (He & Ketterson 1995), and when $h(L, T) > 2$, such as when a hole closes in a monolayer (Jensen 1994). The only constraint is that the free surface at the monolayer tip varies over a lengthscale long compared to the fluid depth.

Suppose the monolayer tip advances slowly with speed $V = O(\epsilon)$. In the frame of the tip, using 'inner' variables defined in § 2.2.1 but with arbitrary film height $h(L, T) = \tilde{h}$ and flux $Q(L, T) = V\tilde{Q}$, lubrication theory shows that beneath the rigid portion of the monolayer tip (at the upstream end of the inner region, with $\tilde{x} \to -\infty$), the streamfunction and the flux satisfy

$$\tilde{\psi}(\tilde{x}, y) \sim \frac{y^3}{\tilde{h}^3}\left[\tilde{h} - 2\tilde{Q}\right] + \frac{y^2}{\tilde{h}^2}\left[-\tilde{h} + 3\tilde{Q}\right], \quad \tilde{Q} \sim -\frac{\tilde{h}^3}{12}\tilde{p}_{\tilde{x}} + \frac{\tilde{h}}{2}, \tag{2.19a,b}$$

so that $\tilde{\psi}(\tilde{x}, \tilde{h}) = \tilde{Q}$, $\tilde{\psi}_y(\tilde{x}, \tilde{h}) = 1$, $\tilde{\psi}(\tilde{x}, 0) = \tilde{\psi}_y(\tilde{x}, 0) = 0$. The surfactant concentration locally satisfies $\tilde{\Gamma} \sim 2\tilde{h}^{-2}(3\tilde{Q} - 2\tilde{h})\tilde{x}$. The local pressure gradient $\tilde{p}_{\tilde{x}}$ in (2.19) is a constant determined by restoring forces acting over long lengthscales. Just ahead of the monolayer (as $\tilde{x} \to \infty$), where the interface is free of tangential stress,

$$\tilde{\psi}(\tilde{x}, y) \sim \frac{\tilde{Q}}{2}\left[-\frac{y^3}{\tilde{h}^3} + \frac{3y^2}{\tilde{h}^2}\right], \quad \tilde{Q} \sim -\frac{\tilde{h}^3}{3}\tilde{p}_{\tilde{x}} \tag{2.20a,b}$$

so that $\tilde{\psi}(\tilde{x}, \tilde{h}) = \tilde{Q}$, $\tilde{\psi}_{yy}(\tilde{x}, \tilde{h}) = 0$, $\tilde{\psi}(\tilde{x}, 0) = \tilde{\psi}_y(\tilde{x}, 0) = 0$. The pressure gradient in (2.20) generally takes a different value to that in (2.19). If the flow ahead of the monolayer tip is quasi-steady (as is the case in Appendix A, for example), $\tilde{Q} = \tilde{h} - 1$ and we recover the upstream and downstream streamfunctions $\psi^{\pm}(y; \tilde{h})$, where

$$\psi^{-}(y; h) = (2 - h)\left(\frac{y^3}{h^3} - \frac{3y^2}{2h^2}\right) + \frac{y^2}{2h}, \quad \psi^{+}(y; h) = -\tfrac{1}{2}(h - 1)\left(\frac{y^3}{h^3} - \frac{3y^2}{h^2}\right). \tag{2.21a,b}$$

Some corresponding velocity profiles are shown in figure 3. The complete range of such transitions can in principle arise under various flow conditions; of particular interest are the cases $h = 1$ (see (2.18*c*)) and $h = h_0 \approx 1.6839$ (Appendix A). The quasi-steady assumption fails if, for example, an unsteady gravity-driven disturbance advances ahead of the monolayer with $\tilde{h} > 1$, and then the more general case (2.19)–(2.20) applies.

To find the Stokes flow and surfactant distribution connecting (2.19) and (2.20), we

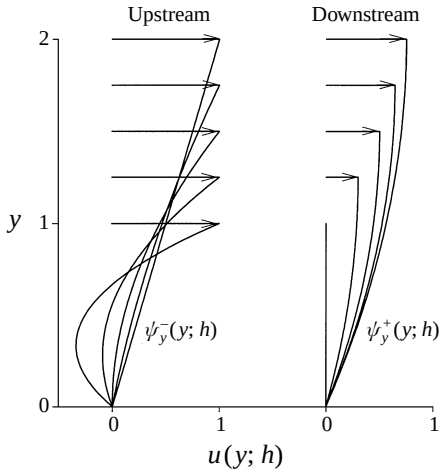

FIGURE 3. Velocity profiles in the frame of the solid boundary, given by (2.21), either side of the leading edge of a monolayer for $h = 1$, 1.25, 1.5, 1.75 and 2: upstream (left) the surface is rigid, advancing with unit speed; downstream (right) the free surface is stress-free. In each case the horizontal flux is $h - 1$.

define a rescaled streamfunction $\Psi(X, Y)$ by

$$\tilde{\psi}(\tilde{x}, y) = \frac{\tilde{Q}}{2}\left[-\frac{y^3}{\tilde{h}^3} + \frac{3y^2}{\tilde{h}^2}\right] + (\tilde{h} - \tfrac{3}{2}\tilde{Q})\Psi(X, Y), \quad \tilde{x} = \tilde{h}X, \quad y = \tilde{h}Y. \quad (2.22a\text{–}c)$$

The pressure transforms according to $\tilde{p} = -3\tilde{h}^{-3}\tilde{Q}\tilde{x} + (\tilde{h} - \frac{3}{2}\tilde{Q})\tilde{h}^{-2}P$. Then, in $-\infty < X < \infty$, $0 \leqslant Y \leqslant 1$, Ψ satisfies

$$\nabla^4\Psi = 0, \quad \Psi(X, 0) = 0, \quad \Psi_Y(X, 0) = 0, \quad \Psi(X, 1) = 0 \qquad (2.23a\text{–}d)$$

where

$$\Psi(X \to -\infty, Y) \sim Y^3 - Y^2, \quad \Psi(X \to \infty, Y) \to 0. \qquad (2.24a,b)$$

The free-surface boundary conditions (cf. (2.16), (2.17)) are

$$\Psi_{YY}(X, 1) = -G_X, \quad \Psi_Y(X, 1) = 1 + \frac{\hat{\mathscr{D}}G_X - \hat{\gamma}}{G}, \quad G(X \to \infty) \to \hat{\gamma}, \quad (2.25a\text{–}c)$$

where $\tilde{\Gamma}(\tilde{x}) = [(\tilde{h} - \frac{3}{2}\tilde{Q})/\tilde{h}]G(X)$, $\tilde{\gamma} = [(\tilde{h} - \frac{3}{2}\tilde{Q})/\tilde{h}]\hat{\gamma}$ and $\tilde{\mathscr{D}} = (\tilde{h} - \frac{3}{2}\tilde{Q})\hat{\mathscr{D}}$. Note that in the flat-film limit $\hat{\gamma} \equiv \tilde{\gamma}$ and $\hat{\mathscr{D}} \equiv \tilde{\mathscr{D}}$. (We have assumed for simplicity that $\tilde{\Gamma} \to \tilde{\gamma}$ as $\tilde{x} \to \infty$, whereas strictly $\tilde{\gamma}$ will be altered slightly from its value at infinity by the flow ahead of the monolayer tip.) Equations (2.23)–(2.25) are solved in §§ 3–5; the scaled streamfunction Ψ is exactly that arising in the flat-film problem described in § 2.2.1.

3. The stick-slip leading-edge Stokes flow

We consider in this section the singular limit of (2.23)–(2.25) (or (2.15)–(2.18) with $\tilde{\mathscr{R}} = 0$) in which there is no contaminant ahead of the monolayer and surface diffusion is negligible, before introducing these effects in § 4 and § 5.

If $\hat{\mathscr{D}} = 0$ and $\hat{\gamma} = 0$, then (2.23)–(2.25) reduce to a stick-slip problem for which

$$\Psi_Y(X < 0, 1) = 1, \quad \Psi_{YY}(X > 0, 1) = 0. \qquad (3.1a,b)$$

In the neighbourhood of the monolayer's leading edge the streamfunction is singular, having the local form (Michael 1958; Richardson 1970; Harper 1992)

$$\Psi \sim Y - 1 + \Lambda r^{3/2} \sin\theta \sin\tfrac{1}{2}\theta, \quad |X| \ll 1, \quad |1 - Y| \ll 1, \tag{3.2}$$

for some constant Λ, where $r = [X^2 + (1-Y)^2]^{1/2}$, $0 \leqslant \theta \leqslant \pi$, $\theta = 0$ along $Y = 1$, $X < 0$ and $\theta = \pi$ along $Y = 1$, $X > 0$. Thus along $Y = 1$, as $|X| \to 0$, we have (3.1) and

$$\Psi_{YY}(X < 0, 1) \sim \Lambda(-X)^{-1/2}, \quad \Psi_Y(X > 0, 1) \sim 1 - \Lambda X^{1/2}. \tag{3.3a,b}$$

From the surface stress distribution we can compute the monolayer concentration using (2.25*a*), so that $G \sim 2\Lambda(-X)^{1/2}$ as $X \to 0-$ and $G \sim -4X + \Upsilon$ as $X \to -\infty$, for some constant Υ given by

$$\Upsilon = \int_{-\infty}^{0} [\Psi_{YY}(X, 1) - 4] \, \mathrm{d}X. \tag{3.4}$$

This implies that the monolayer's leading edge lies an X-distance $\frac{1}{4}\Upsilon$ upstream of the location predicted by thin-film theory, i.e. the quasi-steady monolayer x-length correction is $\frac{1}{4}\Upsilon h(L, T)$ (see § 2.3). Assuming that the pressure satisfies $P \to 0$ as $X \to \infty$, then $P \sim 6X + \Theta$ as $X \to -\infty$ where the constant Θ is given by

$$-\Theta = \int_{-\infty}^{0} [\Psi_{YYY}(X, 0) - 6] \, \mathrm{d}X + \int_{0}^{\infty} \Psi_{YYY}(X, 0) \, \mathrm{d}X. \tag{3.5}$$

The method of matched eigenfunction expansions (Appendix C), in which truncated series expansions for the streamfunction in $X > 0$ and $X < 0$ (C 4) are patched across $X = 0$, provides a relatively simple and direct technique for determining the majority of the flow governed by (2.23), (2.24) and (3.1), although it fails to resolve the details near the singularity. Numerical results obtained with this method are shown in figures 4–6. Application of the Wiener–Hopf technique (Appendix D; Kim & Chung 1984) yields the significant constants in the flow (see for example (D 8)),

$$\Lambda = \sqrt{8/\pi}, \quad \Upsilon = 4\Omega, \quad \Theta = -6\Omega, \quad \Omega \approx 0.20943. \tag{3.6a–d}$$

Eigenfunction expansions for each half of the flow can also be derived by the Wiener–Hopf method, but since the coefficients involve slowly converging infinite products a more direct method of solution is appropriate.

The streamfunction (figure 4*a*) shows the return-flow structure far upstream, which drives a line of weak vortices ahead of the monolayer, the largest of which is shown. This is exactly the streamfunction appropriate to the flat-film problem of § 2.2; for cases in which $\tilde{Q} > 0$ in § 2.3 (such as that shown in figure 11 below), the recirculation is swamped by the mean flux. The horizontal component of the velocity field (figure 5*a*) shows the surface velocity profile, and in particular the high degree of surface compression ($U_X < 0$) just ahead of the monolayer tip. The figure also shows how the return-flow velocity profile decays rapidly to zero essentially within 2 film depths of $X = 0$. Computations of the the vorticity and pressure distributions (figures 4*b* and 5*b*) cannot resolve the details of the stress singularity, but are good approximations of the solution elsewhere. They show that although $\omega = -\nabla^2\Psi = 0$ along the free surface ahead of the monolayer, vorticity can diffuse a short distance ahead of $X = 0$, and that the pressure has a surprisingly complex distribution in this region.

The tangential stress $\Psi_{YY}(X, 1)$ (figure 6*a*) is singular as $X \to 0-$ (see (3.3*a*)), and is non-monotonic in $X < 0$, having a local minimum value of approximately 3.98

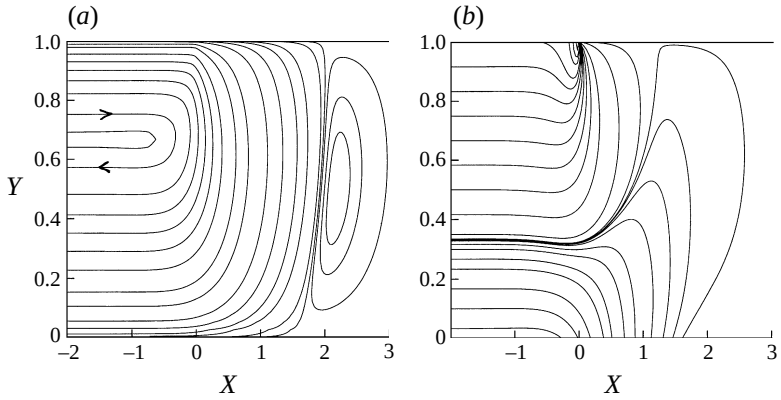

FIGURE 4. The streamfunction $\Psi(X, Y)$ (*a*) and vorticity distibution $-\nabla^2\Psi$ (*b*) of the stick-slip flow; the monolayer lies along $X < 0$, $Y = 1$. One vortex is shown in (*a*), the largest contour value within it is 1.5×10^{-5}. In (*b*), the vorticity increases linearly from -2 to $+4$ far upstream; a few contours are clustered around the zero level; the singularity is evident beneath the monolayer tip at $(0, 1)$.

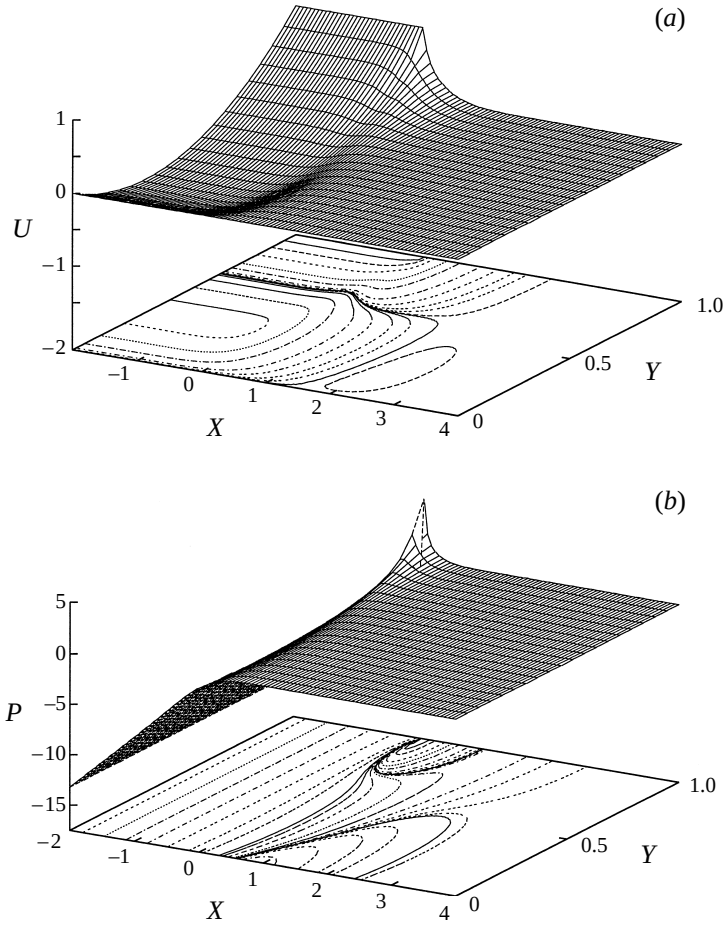

FIGURE 5. (*a*) The horizontal component of the velocity field $U = \Psi_Y(X, Y)$; a few contours are clustered around $U = 0$ to demonstrate the solution's structure for $X > 0$. (*b*) The pressure distribution $P(X, Y)$.

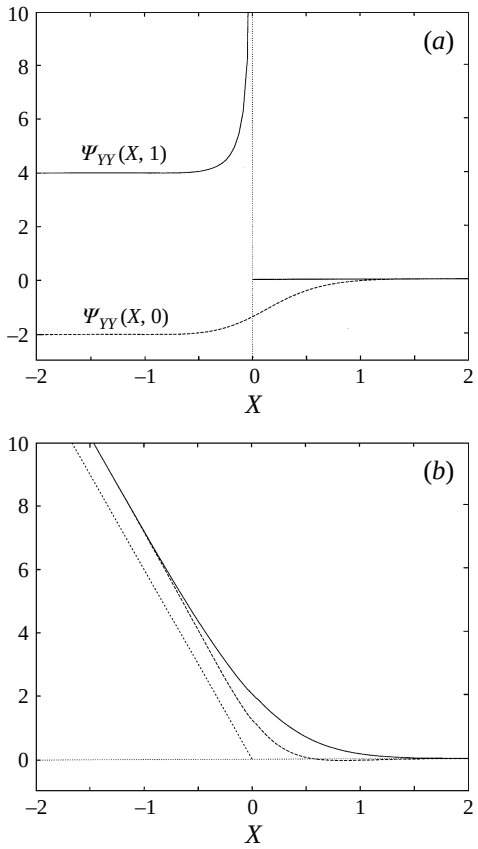

FIGURE 6. The tangential (*a*) and normal (*b*) stresses along $Y = 0$ (dashed) and $Y = 1$ (solid). The straight line in (*b*) is $-6X$. The solid line in (*b*), turned upside down, gives the shape of the free-surface perturbation $\tilde{h}_1$ for a monolayer spreading on a flat film (see (2.17)).

at $X \approx -0.82$. The huge variation in stress at the free surface is strongly localized; in comparison, the tangential stress at the lower boundary rises smoothly from a minimum value of approximately -2.01 near $X \approx -0.86$ up to zero as X increases. Similar stress distributions arise in the related problem of a flow past a stationary splitter plate in a channel (Badr *et al.* 1985). In the neighbourhood of the singularity the normal stress $-P - 2\Psi_{XY}$ at the free surface falls smoothly (figure 6*b*), reaching zero a short distance downstream of the monolayer's leading edge. In the flat-film case (§ 2.2.1) using (2.17), the solid curve in figure 6(*b*) turned upside down gives the shape of the free-surface perturbation $\tilde{h}_1$, which rises smoothly to a uniform value, reaching its maximum value roughly 1.5 film depths ahead of the monolayer tip. The normal stress on the lower boundary is weakly non-monotonic, having a minimum value of -0.049 near $X = 0.85$.

The shape of the interface near the monolayer tip in the flat-film case (figure 6*b*) is to be contrasted to the closely-related die-swell problem in which a jet leaving a nozzle has been predicted to have a singular curvature distribution when surface tension is present (Schultz & Gervasio 1990). No such singularity arises in the case of a spreading monolayer, presumably because different kinematic boundary conditions apply in the two problems. For a spreading monolayer the entire interface can deform in the vertical direction, and there is no difficulty in the interface having small but

finite slope in the neighbourhood of the monolayer tip (at $X = 0$). In the die-swell problem the free-surface slope exiting the die may be non-zero, but the die is constrained to be horizontal.

Figure 6(b) also confirms the prediction of the Wiener-Hopf analysis (see (3.5), (3.6)) that, as $X \to -\infty$, $P \sim 6(X - \Omega)$; similarly, $G \sim -4(X - \Omega)$. We have therefore been able to compute $O(1)$ corrections to the asymptotic boundary conditions for a monolayer on a flat film in (2.17), i.e. $\tilde{p}_0 \sim 6(\tilde{x} - \Omega)$, $\tilde{\Gamma}_0 \sim -4(\tilde{x} - \Omega)$, which again indicate how lubrication theory over-predicts the monolayer length in this case by a distance Ω. Finally, if the only restoring force acting on the interface is surface tension, a simple rescaling of the normal stress distribution along $Y = 1$ in figure 6(b), following (2.22), can be used to smooth the jump in pressure gradient in figure 11(b) below.

4. The effects of weak contaminant in Stokes flow

A small amount of contaminant on the free surface ahead of the monolayer eliminates the stress singularity. Here we examine the resulting Stokes flow in the neighbourhood of the monolayer's leading edge, first by considering (2.23)–(2.25) with $\hat{\mathscr{D}} = 0$, $\hat{\gamma} > 0$. For $\hat{\gamma} \gg 1$ the long-wavelength result (figure 2) is recovered. We link this with Harper's (1992) asymptotic solution for $0 < \hat{\gamma} \ll 1$ (recalled in § 4.2 below) by solving the full nonlinear problem numerically using a boundary-element method (§ 4.1). However, we first examine the far-field asymptotic behaviour of (2.23)–(2.25), since this is necessary if the numerical solution domain is to be truncated at finite values of X.

Far upstream, for $-X \gg \max(\hat{\gamma}, 1)$, an asymptotic expansion of (2.23)–(2.25) yields

$$G(X) \sim -4X - \hat{\gamma}\log(-X), \quad \Psi(X, Y) \sim (Y^3 - Y^2)\left(1 + \frac{\hat{\gamma}}{4X}\right), \qquad (4.1a,b)$$

consistent with (2.12); it indicates that for $\hat{\gamma} > 0$ the shear stress $\Psi_{YY}(X, 1) \sim 4 + (\hat{\gamma}/X)$ lies beneath its asymptotic value of 4 far upstream.

The solution for $X \to \infty$ is determined as follows. Set $G = \hat{\gamma}(1 + \varepsilon g(X))$, for some $\varepsilon \ll 1$, $g = O(1)$, and put $\Psi = \varepsilon\Phi$. After linearizing the free-surface boundary conditions, (2.23)–(2.25) yield $\nabla^4\Phi = 0$ subject to

$$\Phi(X, 0) = 0, \quad \Phi_Y(X, 0) = 0, \quad \Phi(X, 1) = 0, \quad \hat{\gamma}\Phi_{XY}(X, 1) + \Phi_{YY}(X, 1) = 0. \qquad (4.2a\text{–}d)$$

An eigenfunction expansion can be constructed, as in Appendix C, by setting $\Phi(X, Y) = \sum_{n=0}^{\infty} A_n e^{-\omega_n X} E(Y; \omega_n)$, where the eigenvalues ω_n have positive real part and the eigenfunctions are given by (C 1). The mixed boundary condition (4.2d) implies that the ω_n are the roots of $E_{YY}(1, \omega) - \hat{\gamma}\omega E_Y(1, \omega) = 0$, which from (C 3) is equivalent to

$$\hat{\gamma}(\omega^2 - \sin^2\omega) - (2\omega - \sin 2\omega) = 0. \qquad (4.3)$$

Some roots of (4.3) are plotted in figure 7. There is one purely real eigenvalue ω_0, which satisfies $\omega_0 \sim 4/\hat{\gamma}$ as $\hat{\gamma} \to \infty$ (corresponding to a return flow (2.12)), and a sequence of complex eigenvalues ω_n, $n = 1, 2, \ldots$, with increasing real parts, corresponding to vortices. For $\hat{\gamma} \gg 1$ these roots correspond to those of a rigid interface ($E_Y(1, \omega) = 0$); for $\hat{\gamma} \ll 1$, they approach those of a stress-free interface ($E_{YY}(1, \omega) = 0$). For $\hat{\gamma} = 2/t_n$, where $\tan t_n = t_n$ and $t_1 \approx 4.49341$, the purely real eigenvalue ω_0 coalesces with the pair ω_n; for all other values of $\hat{\gamma}$ the pair ω_n has non-zero imaginary part. As $\hat{\gamma}$

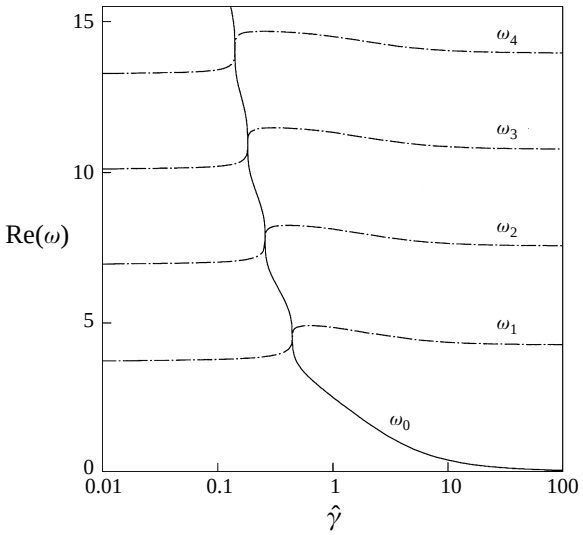

FIGURE 7. The dependence of the real parts of the eigenvalues satisfying (4.3) on $\hat{\gamma}$.

decreases, ω_0 moves up the real axis, jumping abruptly as it passes through these critical points (figure 7). The first such transition represents a sudden qualitative change in the flow structure: for $\hat{\gamma} > 2/t_1 \approx 0.445$, the dominant eigenvalue at large X is ω_0, representing the closure of a return flow (as in figure 1); for $\hat{\gamma} < 2/t_1$, the dominant eigenvalue is ω_1, indicating that the flow drives recirculating vortices similar to those shown in figure 4(*a*).

4.1. *Numerical results using the boundary-element method*

The boundary-element method (BEM) for the Stokes equations exploits the fact that the velocity vector at a point, $\boldsymbol{U}(\boldsymbol{X})$, can be expressed in terms of line integrals involving the velocities and stresses at boundaries:

$$U_k(\boldsymbol{X}) = \int_S U_i(\boldsymbol{Y}) W_{ik}(\boldsymbol{X}, \boldsymbol{Y}) \mathrm{d}S_{\boldsymbol{Y}} - \int_S \tau_i(\boldsymbol{Y}) V_{ik}(\boldsymbol{X}, \boldsymbol{Y}) \mathrm{d}S_{\boldsymbol{Y}}, \tag{4.4}$$

where

$$V_{ik}(\boldsymbol{X}, \boldsymbol{Y}) = -\frac{1}{4\pi}\left(\delta_{ik} \log|\boldsymbol{X} - \boldsymbol{Y}| - \frac{(X_i - Y_i)(X_k - Y_k)}{|\boldsymbol{X} - \boldsymbol{Y}|^2}\right)$$

and

$$W_{ik}(\boldsymbol{X}, \boldsymbol{Y}) = -\frac{1}{\pi}\frac{(X_i - Y_i)(X_j - Y_j)(X_k - Y_k)}{|\boldsymbol{X} - \boldsymbol{Y}|^4} n_j(\boldsymbol{Y}).$$

Here S is the boundary surface and $\tau_i = \{\boldsymbol{T}\}_{ij} n_j$ is the stress vector. If $\boldsymbol{X} \in S$, then $U_k(\boldsymbol{X})$ is replaced with $C_{ik} U_i(\boldsymbol{X})$ ($C_{ik} = \frac{1}{2}\delta_{ik}$ where the interface is smooth) to take into account the jump in stress at the free surface.

We implemented this method using the same discretization as in Halpern & Gaver (1994). The solution domain was truncated, and the resulting rectangular domain had its boundary divided into N 3-point elements; the velocity and stress fields were approximated as quadratic polynomials in terms of a local coordinate system. Equation (4.4) was then replaced by a system of N linear equations

$$\check{H}\check{\boldsymbol{w}} = \check{G}\check{\boldsymbol{t}}, \tag{4.5}$$

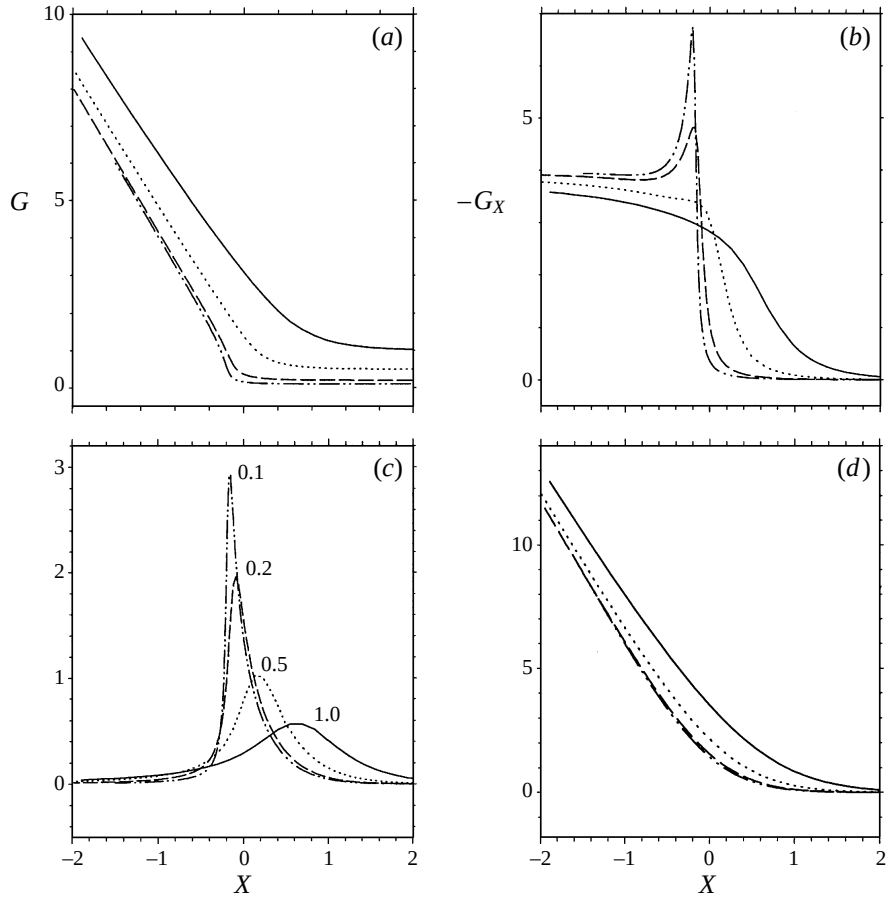

FIGURE 8. BEM results with $\hat{\gamma} = 0.1$ (dot-dashed), 0.2 (dashed), 0.5 (dotted) and 1 (solid): (*a*) the surfactant distribution $G(X)$; (*b*) the surface shear stress $-G_X(X)$; (*c*) surface compression $-\Psi_{XY}(X, 1)$; (*d*) surface normal stress.

where $\check{\boldsymbol{w}}$ and $\check{\boldsymbol{t}}$ denote the velocity and stress vectors at each node point. The elements of matrices $\check{H}$ and $\check{G}$ were computed using methods described in Halpern & Gaver (1994). The linear system (4.5) was solved for the unknown velocities and stresses using Gaussian elimination.

To solve (2.23)–(2.25), the following iterative procedure was used. Given an initial approximation to the surfactant distribution (e.g. from (2.12)), conditions $\check{t}_X = -G_X$ and $V = -\Psi_X = 0$ were imposed along $Y = 1$, so that the unknowns were the horizontal velocity and normal stress components. These were determined by solving (4.5). A new approximation for G was obtained by integrating (2.25*b*) numerically using a Runge–Kutta scheme. This procedure was repeated until a converged solution for G was obtained. At the downstream boundary the dominant terms in the eigenfunction expansion of (4.2) were used; at the upstream boundary the horizontal velocity was prescribed upstream using (4.1). Typically $N = 150$ elements proved adequate.

BEM computations of (2.23)–(2.25) with $\hat{\mathscr{D}} = 0$ are presented in figure 8 for $0.1 \leqslant \hat{\gamma} \leqslant 1$. The shear stress distribution (figure 8*b*) is strongly peaked for $\hat{\gamma} = 0.1$, but decreases monotonically for $\hat{\gamma} = 1$ (over a longer lengthscale), approaching the lubrication theory solution (2.12); this is reflected in the surfactant distribution (figure

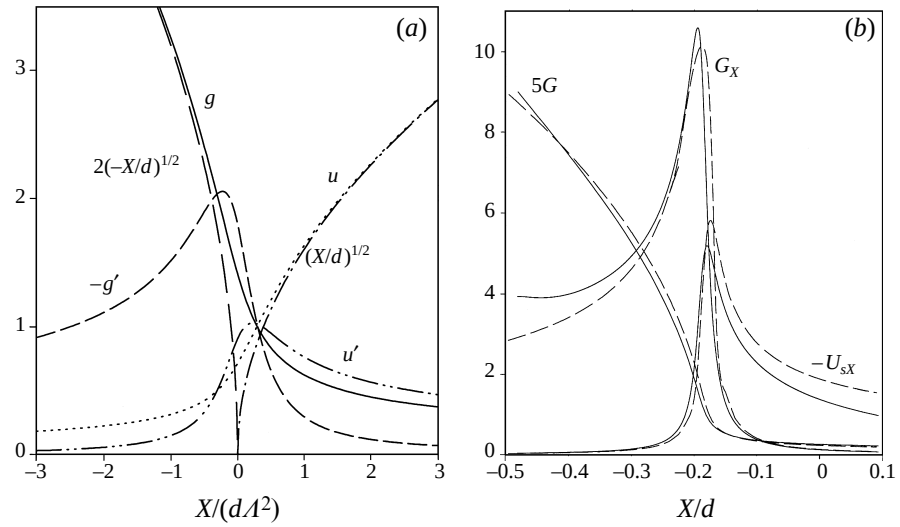

FIGURE 9. The effect of weak contaminant on the singularity: (*a*) shows the surfactant and velocity distributions $g = (2/\phi)^{1/2}$ (solid) and $u = (\phi/2)^{1/2}$ (dotted, see (4.6)), with asymptotes as indicated; the shear stress $-g'$ has a peak upstream of the region of maximum surface compression u'. (*b*) Comparison of boundary-element solutions (solid) with the asymptotic solution (dashed), for $\hat{\gamma} = 0.03$.

8*a*), which develops an inflection point as $\hat{\gamma}$ falls. The surface velocity gradient (figure 8*c*) shows a strong region of surface compression at the monolayer tip; when $\hat{\gamma} = 1$, it has a maximum value of 0.570 which differs from the value predicted by lubrication theory (0.593, using (2.12*a*)) by less than 4 %. The numerics confirm that the vortices vanish when $\hat{\gamma} = 2/t_1$. The normal stress distribution (figure 8*d*) is only weakly dependent on $\hat{\gamma}$, corresponding closely to the stick-slip distribution in figure 6(*b*). The free surface shape is therefore not significantly affected by the degree of surface contamination at low Reynolds numbers. The peak in shear stress vanishes for some $\hat{\gamma}$ very close to that at which the downstream vortices vanish; this relationship is considered in more detail in figure 10 below.

4.2. *Very weak contaminant*

The structure of the stress peak in figure 8(*b*) which is present for $0 < \hat{\gamma} \ll 1$ can be described using the local Stokes-flow solution of Harper (1992). Contaminant influences the stick-slip flow of § 3 profoundly in a small inner region of width $O(\hat{\gamma})$ in the neighbourhood of the singularity at $(0, 1)$. The local streamfunction (3.2) can be written $\Psi \sim (1 - Y)[-1 + \Lambda\ \mathrm{Im}\,(z^{1/2})]$, where $z = -X + \mathrm{i}(1 - Y)$, as $|z| \to 0$. In the presence of weak contamination, this becomes $\Psi \sim (1 - Y)[-1 + \Lambda\ \mathrm{Im}\,\{(z + \mathrm{i}d)^{1/2}\}]$, where $d = \hat{\gamma}/\Lambda^2$ (Harper 1992). This yields surface velocity and concentration distributions, for $X = O(\hat{\gamma})$,

$$\Psi_Y(X,1) \sim 1 - \left(\tfrac{1}{2}\hat{\gamma}\phi\right)^{1/2}, \quad G(X) \sim \left(2\hat{\gamma}/\phi\right)^{1/2}, \quad \phi = \left[1 + \left(X/d\right)^2\right]^{1/2} + (X/d), \tag{4.6a–c}$$

as shown in figure 9(*a*). For $X \gg \hat{\gamma}$, where the free surface is compressed by viscous forces $G \sim (\hat{\gamma}/\Lambda)X^{-1/2}$; for $-X \gg \hat{\gamma}$, where the free surface is clogged, $\Psi_Y \sim 1 - [\hat{\gamma}/(2\Lambda)](-X)^{-1/2}$. These limits match onto the outer stick-slip flow of § 3

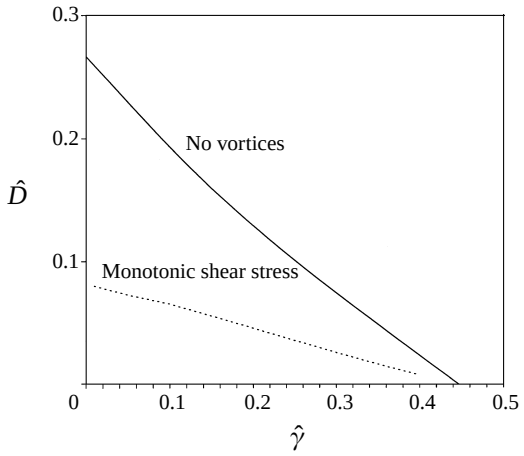

FIGURE 10. Above the upper line (obtained using (5.1)) solutions of (2.23)–(2.25) do not exhibit recirculating vortices; above the lower line the surface shear stress distribution is monotonic.

(denoted here by $\Psi^{(0)}(X, Y)$, $G^{(0)}(X)$, say), provided that ahead of the monolayer, with $\hat{\gamma} \ll X = O(1)$, we use (2.25) to deduce that $G \sim \hat{\gamma}/[1 - \Psi_Y^{(0)}]$. Thus $G \to \hat{\gamma}$ exponentially fast over an $O(1)$ distance ahead of the advancing monolayer. Upstream of the leading edge, for $-X \gg \hat{\gamma}$, the concentration $G^{(0)}$ is unaffected at leading order by the contaminant.

A comparison between BEM results and the small-$\hat{\gamma}$ asymptotics is shown in figure 9 (b); the agreement is quite respectable. Convergence, resolution and round-off constraints prevented the BEM code from tackling substantially smaller values of $\hat{\gamma}$; the asymptotic solution for $\hat{\gamma} = 0.03$ in figure 9(b) is a leading-order local solution that is valid only near the stress peak, and it diverges as expected from the numerical solution further from the regularized singularity. As $\hat{\gamma} \to 0$, the surface shear stress has a maximum value of $(\Psi_{YY})_{max} \sim 3^{3/4}\Lambda^2/(2^{3/2}\hat{\gamma}^{1/2})$ at $X \sim -\hat{\gamma}/(3^{1/2}\Lambda^2)$. The point of maximum surface compression lies just downstream of this, at $X \sim \hat{\gamma}/(3^{1/2}\Lambda^2)$. For $\hat{\gamma} \ll 1$ the contaminant has no significant effect either on the vortices (figure 4a) in $X > 0$ or on the normal stress distribution (figure 8d).

5. Weak surface diffusion

Finally, we briefly consider the additional effect of weak surface diffusion, represented by $\hat{\mathscr{D}}$ in (2.23)–(2.25). If $\hat{\mathscr{D}} > 0$, the eigenvalue relation (4.3) becomes

$$\hat{\gamma}(\omega^2 - \sin^2\omega) - (2\omega - \sin 2\omega)(1 - \omega\hat{\mathscr{D}}) = 0. \tag{5.1}$$

If $\hat{\gamma} = 0$, the eigenvalues are $1/\hat{\mathscr{D}}$ and $\frac{1}{2}\alpha_n$, $\frac{1}{2}\overline{\alpha}_n$ ($n = 1, 2, \ldots$), where $\sin\alpha_n = \alpha_n$ (as in Appendix C); thus the critical condition for the existence of vortices is that $\hat{\mathscr{D}} < 2/\mathrm{Re}\,(\alpha_1) \approx 0.26675$. BEM solutions of (2.23)–(2.25) for $\hat{\gamma} \geqslant 0$, $\hat{\mathscr{D}} > 0$ closely resemble those for $\hat{\mathscr{D}} = 0$ in figure 8. We characterize them by plotting in figure 10 two boundaries in $(\hat{\gamma}, \hat{\mathscr{D}})$-parameter space: one across which the vortices vanish; and one across which the stress distribution first becomes non-monotonic. As either contaminant or diffusion increases in strength, the shear stress becomes monotonic *before* the vortices vanish. This surprising result indicates that it is an abrupt change in surface stress, rather than the presence of a large stress peak, which is sufficient to drive the vortices.

6. Discussion

We have investigated the Stokes flow in the neighbourhood of the leading edge of a surfactant monolayer spreading on a thin fluid layer. There is an integrable stress singularity at the monolayer tip which may be smoothed over short lengthscales by either weak surface contamination (arising from a pre-existing monolayer) or surface diffusion. The singularity, even when smoothed, can yield highly non-uniform surface shear-stress distributions (e.g. figures 8*b*, 9*b*) and surface velocity gradients (figures 8*c*, 9*b*) which cannot be described by conventional thin-film theory. In contrast, the normal stress distribution (and hence the free surface shape) remains a monotonic function that varies smoothly on an $O(H^*)$ lengthscale, where H^* is the undisturbed film thickness (figures 6*b*, 8*d*). In conjunction with a strong gravitational field that suppresses free-surface deformations, the non-uniform stress distribution at the monolayer tip generates a train of Moffatt vortices in the fluid immediately ahead of the monolayer (figure 4*a*) over an $O(H^*)$ lengthscale.

Existing predictions of the length of a spreading monolayer are therefore in error by at least $O(H^*)$. For example, neglecting the effects of gravity and inertia, the dimensional length at dimensional time t^* of a localized, non-diffusing, planar monolayer strip of total mass $M^* = \int_0^{L^*} \Gamma^* \, \mathrm{d}x^*$ is given at leading order by

$$L^*(t^*) \sim L_0^*(t^*) = \left(\upsilon H^* M^* A^* t^*/\mu^*\right)^{1/3} \tag{6.1}$$

with $\upsilon = 12$ (see the spreading-strip solution in Jensen & Grotberg 1992). To estimate the importance of transient effects in this large-time approximation one can consider the rate of decay of perturbations to the self-similar solution: with the location of the symmetry line $x = 0$ fixed, these are $O(t^{*-2/3})$, essentially because the similarity solution is independent of the time origin (Grundy & McLaughlin 1982; King & Please 1986). We showed in §§ 2–3 and Appendix A that in an asymptotically uniform approximation we must first include two additional corrections to (6.1), both larger than $O(t^{*-2/3})$, namely

$$L^*(t^*) \sim L_0^*(t^*) - 2\vartheta H^* \left(\frac{\mu^* L_{0t^*}^*}{\sigma_0^*}\right)^{-1/3} - \tfrac{1}{4}\Upsilon H^* h_L. \tag{6.2}$$

The second term on the right of (6.2), which scales like $t^{*2/9}$ for a strip, arises from capillary effects at the shock associated with σ_0^*, the mean surface tension of the film (Appendix A, figure 11; $\vartheta \approx 0.39$); this term depends on the capillary number $Ca = \mu^* L_{0t^*}^*/\sigma_0^*$, which is typically small. The final term in (6.2) represents the effects of the viscous stress singularity (reflected by $\Upsilon \approx 0.84$, computed using the Wiener–Hopf technique; see (3.6) and Appendix D) coupled to the local free-surface shape, which is determined here by capillary forces (so that $h_L = h_0 \approx 1.68$, see § 2.3 and Appendix A).

If restoring forces (such as gravity) are sufficiently strong for the free surface to be flat (e.g. for sufficiently large $\mathscr{G}$ or t^*, § 2.2), the leading-order estimate of monolayer length is instead given by (6.1) with $\upsilon = 9/4$ (see (2.10)), with corrections given by (6.2) with $\vartheta = 0$ and $h_L = 1$. If the film deforms appreciably under gravity (i.e. for $\mathscr{G} = O(1)$, $\mathscr{T} = O(1)$), $L_0^*(t^*)$ must be determined by solving (2.6), (2.7) numerically; we showed in § 2.3 that the final term in (6.2) applies to such transient (non-self-similar) flows, where h_L is the slowly varying film height at which lubrication theory predicts that $\Gamma = 0$.

If, on a flat film, weak contaminant is present, represented by S_∞^* (the surface-tension reduction due to contaminant), the deposited monolayer's leading edge must

be followed as a Lagrangian trajectory (Grotberg, Halpern & Jensen 1995), but if S^*_∞ is sufficiently small we may still use (6.1) to approximate the Eulerian flow. The evolving role of contaminant at the monolayer tip is described by an inverse contaminant capillary number $\tilde{\gamma} = S^*_\infty/(\mu^* L^*_{0t^*})$, which rises in magnitude as the monolayer spreads. At relatively early times, for which $\tilde{\gamma} \ll 1 \ll L^*_0/H^*$, the asymptotic solution of Harper (1992) applies (see § 4.2) in conjunction with the stick-slip flow of § 3, and the surface shear stress has a large peak over a very short $O(\tilde{\gamma}H^*)$ lengthscale (as in figure 9). Once $\tilde{\gamma} = O(1)$, the surface shear stress distribution becomes smoother, as shown by the BEM solutions in figure 8. The vortices ahead of the monolayer vanish abruptly once $\tilde{\gamma} > 0.445$ if surface diffusion is negligible (§ 4), although they can exist even when the surface shear stress distribution is monotonic, as long as it varies sufficiently rapidly (figure 10). This surprising feature is enhanced when surface diffusion is stronger. Once $1 \leqslant \tilde{\gamma} \ll L^*_0/H^*$, lubrication theory applies throughout the flow (figure 2), and (2.12) may be used at the monolayer tip. Subsequently, contaminant effects become increasingly important, since flow disturbances can ultimately spread rapidly as a diffusive 'compression wave' through the contaminant monolayer (Grotberg *et al.* 1995), so that the lengthscale of the self-similar Eulerian flow becomes $(H^* S^*_\infty t^*/\mu^*)^{1/2}$ (Bois & Panaiotov 1995).

Inertial effects are potentially important early in spreading, where they can generate significant free-surface deformation near the monolayer tip, and they are considered in detail in Part 2 of this study (Jensen 1998). There it is shown that two necessary conditions for the stick-slip or BEM flows described herein to be valid approximations are

$$t^* \gg \frac{\rho^* H^* L^*_0}{\mu^*} \quad \text{and} \quad \tilde{\gamma}\tilde{\mathscr{R}} \equiv \frac{\rho^* H^* S^*_\infty}{\mu^{*2}} \ll 1. \tag{6.3a,b}$$

The latter condition (see figure 10 of Jensen 1998) is stringent, requiring extremely low levels of contaminant (for a 1 mm layer of water, for example, we require $S^*_\infty \ll 10^{-3}$ g s^{-2}, which should be compared with the surface tension of clean water in air $\sigma^*_0 \approx 72$ g s^{-2}); if (6.3*b*) is violated, then inertially dominated flow at the monolayer tip may evolve directly into a flow described by lubrication theory, and the present Stokes flows do not arise.

When gravity is sufficiently strong, the flow structure is quite unlike that described in previous studies of spreading insoluble monolayers (Gaver & Grotberg 1990; Jensen & Grotberg 1992; Jensen 1995): there is a strong region of recirculation along the length of the monolayer and a weaker gravity-driven flow over long lengthscales ahead of the fluid layer (Appendix B). Flow disturbances due to the presence of the spreading monolayer may be felt at a given location long before the surfactant reaches this point. The return-flow structure arising when the free surface is constrained to be almost flat (figure 1) also has important consequences for the transport of soluble surfactant or a passive solute (Jensen & Grotberg 1993; Jensen, Halpern & Grotberg 1994). The effect of suppressing free-surface deformations is to force the cross-sectionally averaged flow rate at any location to be zero to leading order. Advection of surfactant in the bulk becomes very weak compared to surface transport of material that has adsorbed at the free surface. For highly soluble surfactants on thin, flat films, surface tension gradients are therefore likely to play a minor role compared to horizontal bulk diffusion or possibly shear dispersion.

The results of the present study for flows in rectangular domains can be used to help interpret the role of the stress singularity in more complex flow geometries. This is particularly important because such singularities present a signficant challenge to

most numerical solution schemes, where they may have non-local effects (Floryan & Czechowski 1995). Unless special precautions are taken, such as the inclusion of 'singular' boundary or finite elements, the stress distribution cannot be properly resolved. Such deficiencies appear to be present, for example, in the computations of Bel Fdhila & Duineveld (1996), which show peaks in vorticity and pressure at the tip of the stagnant cap at the rear of a bubble across a range of Reynolds numbers, and in the computations of Pawar & Stebe (1996), which indicate the existence of a probable stress singularity associated with the abrupt change in boundary conditions at phase boundaries in monolayers covering bubbles in extensional flows. As we have seen in detail here, the introduction of weak contaminant or diffusion provides a simple means for obtaining physically self-consistent solutions (see also Cuenot, Magnaudet & Spennato 1997).

D. H. acknowledges the support of the NSF EPSCoR in Alabama.

Appendix A. Weak restoring forces: a freely deforming interface

If $\mathscr{G} = 0$ in (2.6), so that the only restoring force acting on the free surface is surface tension, the leading-edge condition (2.7) is replaced by an advancing discontinuity in height and shear stress (Borgas & Grotberg 1988; Park 1992),

$$h = \begin{cases} 2 \\ 1, \end{cases} \quad \Gamma = \begin{cases} -\frac{1}{2}L_T(\bar{X} - L) & \text{for } \bar{X} \to L(T)- \\ 0 & \text{for } \bar{X} > L(T), \end{cases} \tag{A 1}$$

the analogue of (2.11). Since the monolayer advances slowly, with speed $V = \epsilon L_T$ (i.e. dimensional speed $V^* = S^* V/\mu^*$), the jump in film height is smoothed by surface tension over a long $\tilde{x}$-lengthscale of $O(Ca^{-1/3})$ (Jensen & Grotberg 1992), where the local capillary number $Ca \equiv V/\mathscr{S} = V^*\mu^*/\sigma_0^*$ is small since $\mathscr{S} > 1$ and $V = O(\epsilon)$. Setting $x = (L/\epsilon) + (\hat{x}/\hat{\epsilon})$, $\tilde{\Gamma} = \hat{\Gamma}/\hat{\epsilon}$, where $\hat{\epsilon} = Ca^{1/3}$, a thin-film approximation of (2.1)–(2.5) yields, for the capillary transition region

$$\tfrac{1}{6}h^3 h_{\hat{x}\hat{x}\hat{x}} = h - 2, \quad \tfrac{1}{2}h^2\hat{\Gamma}_{\hat{x}} = h - 3 \quad (\hat{x} < 0), \tag{A 2}$$

$$\tfrac{1}{3}h^3 h_{\hat{x}\hat{x}\hat{x}} = h - 1, \qquad \hat{\Gamma} = 0 \qquad (\hat{x} > 0) \tag{A 3}$$

(Jensen & Grotberg 1992). Since this region is short compared to the length of the monolayer, variations in surface tension are small in comparison to its large mean value.

The solution of (A 2)–(A 3) is shown in figure 11. The film height decreases monotonically from 2 to $h_0 \approx 1.6839$ in $\hat{x} < 0$, and has a wavy structure as it falls from h_0 to $h = 1$ far downstream. For $\hat{x} \to -\infty$, the surfactant distribution has the form $\hat{\Gamma} \sim -\frac{1}{2}\hat{x} + \vartheta$ where $\vartheta \approx 0.3896$, implying that capillarity shortens the monolayer by an $\tilde{x}$-distance $2\vartheta/\hat{\epsilon}$ (see (6.2)). Across $\hat{x} = 0$, this thin-film approximation predicts jumps in shear stress, pressure gradient (the jump in $h_{\hat{x}\hat{x}\hat{x}}$ in figure 11*b*) and velocity profile (given by $\hat{\psi} \to \psi^{\pm}(y; h_0)$ as $\hat{x} \to 0\pm$; see (2.21) and figure 3).

The Navier–Stokes problem over lengthscales shorter than $O(Ca^{-1/3})$, in the domain $-\infty < \tilde{x} < \infty$, $0 \leqslant y \leqslant h_0$, is then readily obtained using a similar procedure to that in § 2.2.1, taking as its upstream and downstream conditions the local solutions of (A 2), (A 3) across $\hat{x} = 0$, which is equivalent to the conditions described in § 2.3. Normal stresses in the Navier–Stokes problem generate corrections to the film height which arise formally at $O(\hat{\epsilon}^3)$, which smooth the jump in the third derivative of h across $\hat{x} = 0$. These would therefore be almost imperceptible in Stokes flows, but an

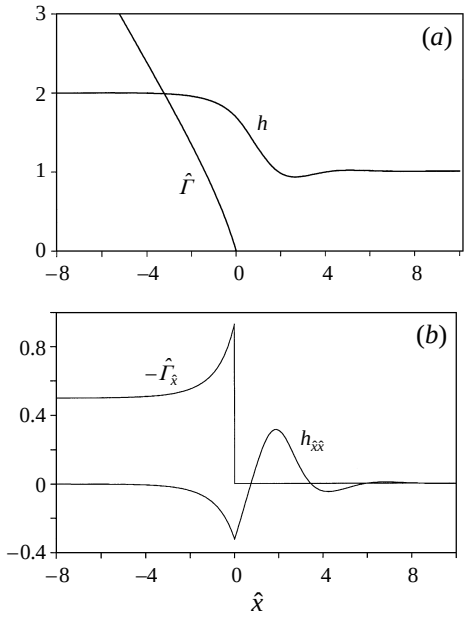

FIGURE 11. The capillary transition region, in the small-capillary-number limit, given by lubrication theory (A 2), (A 3): (*a*) $\hat{\Gamma}(\hat{x})$ and film height $h(\hat{x})$; (*b*) $-\hat{p}(\hat{x}) = h_{\hat{x}\hat{x}\hat{x}}$ and the surface shear stress $-\hat{\Gamma}_{\hat{x}}$. At $\hat{x} = 0$, $h_{\hat{x}} \approx -0.3091$ and $h_{\hat{x}\hat{x}\hat{x}} \approx -0.3262$.

inertially-generated Reynolds ridge (see Jensen 1998) may be observable near $h \approx 1.7$ if the monolayer spreads sufficiently rapidly.

Appendix B. The gravity-driven flow ahead of the monolayer

Ahead of the monolayer, where $\Gamma = 0$ in $X > L(T)$, $h_T = \frac{1}{3}\mathscr{G}(h^3 h_X)_X$ from (2.6*a*). Perturbations to the film height of $O(1/\mathscr{G})$, driven by the monolayer, diffuse quickly ahead of it over a lengthscale $(\mathscr{G}T)^{1/2}$. We assume $(\mathscr{G}T)^{1/2} \gg L(T)$, and introduce an outer variable $X = \mathscr{G}^{1/2}Z$, and again expand setting $h \sim 1 + \hat{h}(Z, T)$, $|\hat{h}| \ll 1$, to give $\hat{h}_T = \frac{1}{3}\hat{h}_{ZZ}$. At the upstream end of this region, $\hat{h}(0, T) = \mathscr{H}(T)/\mathscr{G}$, to match with the outer limit of the flow beneath the monolayer (2.8*a*). We seek similarity solutions dependent on the variable $\Xi = Z/T^{1/2}$ of the form $\hat{h}(Z, T) = \mathscr{G}^{-1}\mathscr{H}(T)H(\Xi)$. $\mathscr{H}(T)$ must be found from a global mass balance of fluid. Assuming $\int_0^L \Gamma_0 \, \mathrm{d}X = M =$ constant and using (2.8*a*), we have

$$0 = \mathscr{G}\int_0^\infty (h-1)\,\mathrm{d}X = \mathscr{G}\left\{\int_0^L (h-1)\,\mathrm{d}X + \int_L^\infty (h-1)\,\mathrm{d}X\right\} \tag{B 1}$$

$$\sim \left[\mathscr{H}(T)L(T) - \tfrac{3}{2}M\right] + \mathscr{H}(T)(\mathscr{G}T)^{1/2}\int_0^\infty H(\Xi)\,\mathrm{d}\Xi. \tag{B 2}$$

Since $(\mathscr{G}T)^{1/2} \gg L(T)$, the dominant balance must be $\mathscr{H}(T) = O(M/(\mathscr{G}T)^{1/2})$. The film depth in $X \geqslant 0$ can then be written as a composite expansion over long lengthscales for $\mathscr{G} \gg 1$,

$$h(X, T) \sim 1 + \frac{3}{2\mathscr{G}}\left[M\left(\frac{3}{\pi\mathscr{G}T}\right)^{1/2}\exp\left\{-\frac{3X^2}{4\mathscr{G}T}\right\} - \Gamma_0\right], \tag{B 3}$$

where Γ_0 is a fixed-mass solution of (2.9). The 'kink' in h near $X = L$ (as $\Gamma_0 \to 0$) may be smoothed using numerical solutions such as that shown in figure 6(*b*).

Appendix C. Matched eigenfunction expansions

Let $\{\alpha_n\}_{n=1}^{\infty}$ be the set of roots in the upper right-hand quadrant of the complex plane of $\sin\alpha = \alpha$, and $\{\beta_n\}_{n=1}^{\infty}$ be the set of roots of $\sin\beta + \beta = 0$. We define the following basis functions:

$$E(Y;\lambda) = (1-Y)(\sin\lambda)\sin\lambda Y - \lambda Y \sin[\lambda(1-Y)], \tag{C 1}$$

$$F(Y;\lambda) = 2\lambda[\lambda\cos\lambda(1-Y) - (\sin\lambda)\cos\lambda Y]. \tag{C 2}$$

Writing $D \equiv \partial_Y$, these satisfy $(D^2+\lambda^2)E = F$, $(D^2+\lambda^2)F = 0$, so that $(D^2+\lambda^2)^2 E = 0$, and $E(0;\lambda) = 0$, $DE(0;\lambda) = 0$, $E(1;\lambda) = 0$. Note that $E\left(Y;\overline{\lambda}\right) = \overline{E(Y;\lambda)}$, $F\left(Y;\overline{\lambda}\right) = \overline{F(Y;\lambda)}$, where a bar denotes complex conjugate, and that

$$D^2E(1;\lambda) = \lambda[2\lambda - \sin 2\lambda], \quad DE(1;\lambda) = \lambda^2 - \sin^2\lambda. \tag{C 3}$$

It follows that $f(X,Y;\lambda) = E(Y;\lambda)\mathrm{e}^{\pm\lambda X}$ is a separable (Fadle–Papkovitch) eigenfunction of the biharmonic equation $\nabla^4 f = 0$, satisfying $f(X,0) = 0$, $f_Y(X,0) = 0$, $f(X,1) = 0$. If f represents a streamfunction, then $\nabla^2 f = F(Y;\lambda)\mathrm{e}^{\pm\lambda X}$ represents the corresponding negative vorticity.

The streamfunction satisfying (2.23), (2.24), (3.1) can be written

$$\Psi(X,Y) = \begin{cases} \displaystyle\sum_{n=-\infty}^{\infty} A_n E(Y;\lambda_n)\mathrm{e}^{-\lambda_n X}, & X > 0 \\ Y^3 - Y^2 + \displaystyle\sum_{n=-\infty}^{\infty} B_n E(Y,\mu_n)\mathrm{e}^{\mu_n X}, & X < 0 \end{cases} \tag{C 4}$$

where the λ_n satisfy $\sin 2\lambda = 2\lambda$, i.e. $\lambda_n = \frac{1}{2}\alpha_n$ for $n = 1,2,3,\ldots$, the μ_n satisfy $\sin^2\mu = \mu^2$, i.e. $\mu_{2m-1} = \beta_m$, $\mu_{2m} = \alpha_m$ for $m = 1,2,3,\ldots$, and where $\lambda_{-n} = \overline{\lambda_n}$, $\mu_{-n} = \overline{\mu_n}$, $A_{-n} = \overline{A_n}$, $B_{-n} = \overline{B_n}$, ensuring that Ψ is real. The corresponding vorticity distribution is given by $\omega = -\nabla^2\Psi$, where

$$\omega(X,Y) = \begin{cases} -\displaystyle\sum_{-\infty}^{\infty} A_n F(Y;\lambda_n)\mathrm{e}^{-\lambda_n X}, & X > 0, \\ -(6Y-2) - \displaystyle\sum_{-\infty}^{\infty} B_n F(Y,\mu_n)\mathrm{e}^{\mu_n X}, & X < 0. \end{cases}$$

We follow Schultz & Gervasio (1990) in constructing a vector eigensystem, by defining

$$\boldsymbol{x}(Y;\lambda) = \begin{pmatrix} E(Y;\lambda) \\ F(Y;\lambda) \end{pmatrix}, \quad \boldsymbol{M} = \begin{pmatrix} D^2 & -1 \\ 0 & D^2 \end{pmatrix}, \quad \text{so} \quad \boldsymbol{M}\cdot\boldsymbol{x} = -\lambda^2\boldsymbol{x}.$$

Under the inner product $\langle \boldsymbol{x},\boldsymbol{y}\rangle = \int_0^1 \boldsymbol{x}\cdot\overline{\boldsymbol{y}}\,\mathrm{d}Y$, the adjoint system, for which $\langle \boldsymbol{x},\boldsymbol{M}\boldsymbol{y}\rangle = \langle \boldsymbol{M}^\dagger\boldsymbol{x},\boldsymbol{y}\rangle$, is

$$\boldsymbol{x}^\dagger(Y;\overline{\lambda}) = \begin{pmatrix} F(Y;\overline{\lambda}) \\ E(Y;\overline{\lambda}) \end{pmatrix}, \quad \boldsymbol{M}^\dagger = \begin{pmatrix} D^2 & 0 \\ -1 & D^2 \end{pmatrix}, \quad \text{so} \quad \boldsymbol{M}^\dagger\cdot\boldsymbol{x}^\dagger = -\overline{\lambda}^2\boldsymbol{x}^\dagger.$$

Then for any eigenvalue pair λ_m and λ_n, $(\lambda_n^2 - \lambda_m^2)\left\langle \boldsymbol{x}(Y;\lambda_n), \boldsymbol{x}^\dagger\left(Y;\overline{\lambda_m}\right)\right\rangle = 0$.

At $X = 0$ we match the vectors $(\Psi, -\omega)^T$ and $(\Psi_X, -\omega_X)^T$, so that

$$\sum_{-\infty}^{\infty} B_n \boldsymbol{x}(Y;\mu_n) + \boldsymbol{R} = \sum_{-\infty}^{\infty} A_n \boldsymbol{x}(Y;\lambda_n), \quad \sum_{-\infty}^{\infty} \mu_n B_n \boldsymbol{x}(Y;\mu_n) = \sum_{-\infty}^{\infty} -\lambda_n A_n \boldsymbol{x}(Y;\lambda_n),$$

where $\boldsymbol{R} = (Y^3 - Y^2, 6Y - 2)^T$. Taking the inner product of each sum with $\boldsymbol{x}^\dagger(Y;\overline{\lambda_m})$ and eliminating A_m yields an infinite linear system,

$$\sum_{-\infty}^{\infty} B_n(\lambda_m + \mu_n) \left\langle \boldsymbol{x}(Y;\mu_n), \boldsymbol{x}^\dagger(Y;\overline{\lambda_m}) \right\rangle = -\lambda_m \left\langle \boldsymbol{R}, \boldsymbol{x}^\dagger(Y;\overline{\lambda_m}) \right\rangle.$$

This is truncated, and the resulting linear system is solved to find the B_n and hence the A_n. Because of the singularity, both expansions for the streamfunction fail to converge very close to $X = 0$, although the estimates of the constants in (3.6) converged slowly to their exact values as N was increased. The numerical scheme was limited by the accuracy with which the integrals of the higher-order eigenfunctions could be computed. With 128 eigenfunctions, $\Lambda_0 \approx 1.6$, and $\Theta_0 \approx -1.18$, in reasonable agreement with (3.6). Figure 4 was plotted using $N = 64$.

Appendix D. Wiener–Hopf solution of the leading-edge Stokes flow

We sketch here the application of the Wiener–Hopf technique to the solution of (2.23), (2.24), (3.1). Details of the method may be found in Noble (1958), Richardson (1970, although there is an error in his calculation of the stress singularity, see for example Tanner & Huang 1993), Porter & Dore (1974) and Kim & Chung (1984). The singularity at the monolayer's leading edge is as given by (3.1)–(3.3); the constants Λ, Υ and Θ (see (3.2)–(3.5)) are to be determined.

Define the Fourier transform of the streamfunction $\Psi(X, Y)$ and its inverse to be

$$\hat{\Psi}(\omega, Y) = \int_{-\infty}^{\infty} \Psi(X, Y) \mathrm{e}^{\mathrm{i}\omega X} \, \mathrm{d}X, \quad \Psi(X, Y) = \frac{1}{2\pi} \int_{-\infty}^{\infty} \hat{\Psi}(\omega, Y) \mathrm{e}^{-\mathrm{i}\omega X} \, \mathrm{d}\omega.$$

The biharmonic equation becomes $\hat{\Psi}_{YYYY} - 2\omega^2 \hat{\Psi}_{YY} + \omega^4 \hat{\Psi} = 0$, so the solution satisfying $\hat{\Psi}(\omega, 0) = 0$, $\hat{\Psi}_Y(\omega, 0) = 0$, $\hat{\Psi}(\omega, 1) = 0$ is $\hat{\Psi}(\omega, Y) = A(\omega)\hat{F}(Y;\omega)$ where

$$\hat{F}(Y;\omega) \equiv (1 - Y)\sinh\omega \sinh\omega Y - \omega Y \sinh\{\omega(1 - Y)\}, \tag{D 1}$$

so that $\hat{F}_Y(1;\omega) = \omega^2 - \sinh^2\omega$ and $\hat{F}_{YY}(1;\omega) = \omega(2\omega - \sinh 2\omega)$. We re-state (3.1) as

$$\Psi_Y(X, 1) = \mathrm{e}^{\epsilon X} \quad (X < 0), \quad \Psi_{YY}(X, 1) = 0 \quad (X > 0), \tag{D 2}$$

introducing some small, positive ϵ which will tend to zero at the end of the calculation, to ensure that Fourier transforms can be properly defined. We define the half-range transforms $\hat{\Psi}^+(\omega, Y) = \int_0^\infty \Psi(X, Y)\mathrm{e}^{\mathrm{i}\omega X} \, \mathrm{d}X$, $\hat{\Psi}^-(\omega, Y) = \int_{-\infty}^0 \Psi(X, Y)\mathrm{e}^{\mathrm{i}\omega X} \, \mathrm{d}X$, so that $\hat{\Psi}(\omega, Y) = \hat{\Psi}^+(\omega, Y) + \hat{\Psi}^-(\omega, Y)$, where $\hat{\Psi}^+$ is analytic for all ω, and certainly for $\omega \in R^+ \equiv \{\omega : \mathrm{Im}\,\omega > -\epsilon\}$, and $\hat{\Psi}^-$ is analytic in $R^- \equiv \{\omega : \mathrm{Im}\,\omega < \epsilon\}$. Thus from (3.1), (3.3), using standard asymptotic properties of Fourier integrals,

$$\hat{\Psi}^-_{YY}(\omega, 1) \sim \Lambda\omega^{-1/2}\mathrm{e}^{-\mathrm{i}\pi/4}\Gamma(\tfrac{1}{2}), \qquad |\omega| \to \infty, \quad \mathrm{Im}\,\omega < 0, \tag{D 3}$$

$$\hat{\Psi}^+_{Y}(\omega, 1) \sim \mathrm{i}\omega^{-1} - \Lambda\omega^{-3/2}\mathrm{e}^{3\pi\mathrm{i}/4}\Gamma(\tfrac{3}{2}), \quad |\omega| \to \infty, \quad \mathrm{Im}\,\omega > 0. \tag{D 4}$$

The boundary conditions (D 2) become $\hat{\Psi}_Y^-(\omega,1) = 1/(\epsilon+\mathrm{i}\omega)$, $\hat{\Psi}_{YY}^+(\omega,1) = 0$, so that

$$\hat{\Psi}_Y^+(\omega,1) = A(\omega)\left[\omega^2 - \sinh^2\omega\right] - (\epsilon+\mathrm{i}\omega)^{-1}, \quad \hat{\Psi}_{YY}^-(\omega,1) = A(\omega)\omega\left[2\omega - \sinh 2\omega\right]. \tag{D 5}$$

Eliminating $A(\omega)$ from (D 5),

$$\hat{\Psi}_Y^+(\omega,1) + \hat{\Psi}_{YY}^-(\omega,1)B(\omega) = -\frac{1}{\epsilon+\mathrm{i}\omega} \quad \text{where} \quad B(\omega) = \frac{\sinh^2\omega - \omega^2}{\omega(2\omega - \sinh 2\omega)}. \tag{D 6}$$

We then set $B(\omega) = B^+(\omega)B^-(\omega)$, where $B^\pm(\omega)$ is regular and non-zero in $R^\pm$: the appropriate decomposition is

$$B^\pm(\omega) = \mp\frac{2}{(5\pm 3)}\mathrm{e}^{\pm N(\omega)}\prod_{n=1}^{\infty}\frac{(1\pm\omega/\alpha_n)(1\mp\omega/\overline{\alpha}_n)(1\pm\omega/\beta_n)(1\mp\omega/\overline{\beta}_n)}{(1\pm 2\omega/\alpha_n)(1\mp 2\omega/\overline{\alpha}_n)}$$

(Porter & Dore 1974), where $\{\pm\alpha_n\}_{n=0}^{n=\infty}$ and their complex conjugates $\{\pm\overline{\alpha}_n\}$ are the roots of $\sinh\alpha = \alpha$, with $0 < \arg(\alpha_n) < \frac{1}{2}\pi$ and $|\alpha_n| < |\alpha_{n+1}|$, and $\{\beta_n\}_{n=0}^{\infty}$ are the corresponding roots of $\sinh\beta + \beta = 0$. The exponential terms are required to ensure convergence as $\omega\to\infty$, so that $N(\omega) = (2\mathrm{i}\omega/\pi)\log 2$ and then

$$B^+(\omega) \sim -\mathrm{e}^{\mathrm{i}\pi/4}/(2\sqrt{2}\,\omega^{1/2}) \quad \text{as} \quad \omega\to\infty, \quad \arg(\omega) < \pi, \tag{D 7}$$

a result which can be obtained by exploiting the generalized Gamma (or factorial) function defined by Smith-White & Buchwald (1964); see for example Foote & Buchwald (1985) and references therein. We note that $B^-(\overline{\omega}) = -4\overline{B^+(\omega)}$, $B^-(-\omega) = -4B^+(\omega)$, $\overline{B^-(\overline{\omega})} = B^-(-\omega)$ and $B_\omega^-(0) = 4B_\omega^+(0) = -\mathrm{i}\Omega$ where

$$\Omega = \frac{2\log 2}{\pi} + \mathrm{i}\sum_{n=1}^{\infty}\left\{\left(\frac{1}{\alpha_n} - \frac{1}{\overline{\alpha}_n}\right) - \left(\frac{1}{\beta_n} - \frac{1}{\overline{\beta}_n}\right)\right\} \approx 0.20943. \tag{D 8}$$

This is in accordance with Kim & Chung (1984), who computed 2Ω as 0.4188.

Thus, from (D 6)

$$\frac{\hat{\Psi}_Y^+(\omega,1)}{B^+(\omega)} + \hat{\Psi}_{YY}^-(\omega,1)B^-(\omega) = -\frac{1}{\epsilon+\mathrm{i}\omega}\frac{1}{B^+(\omega)} = C(\omega), \tag{D 9}$$

say. We then seek the decomposition $C(\omega) = C^+(\omega) + C^-(\omega)$, where $C^\pm(\omega)$ is regular in $R^\pm$. This is obtained using a standard contour integral method (Noble 1958). The residue from the single pole at $\zeta = \mathrm{i}\epsilon$ gives $C^-(\omega) = \mathrm{i}(\omega - \mathrm{i}\epsilon)^{-1}/B^+(\mathrm{i}\epsilon) \sim -4\mathrm{i}/\omega$ as $\epsilon\to 0$, so from (D 9), $C^+(\omega)B^+(\omega) = (\mathrm{i}/\omega)\left[1 + 4B^+(\omega)\right]$. It follows from (D 9) that

$$\frac{\hat{\Psi}_Y^+(\omega,1)}{B^+(\omega)} - C^+(\omega) = C^-(\omega) - \hat{\Psi}_{YY}^-(\omega,1)B^-(\omega) = H(\omega), \tag{D 10}$$

for some analytic, bounded function $H(\omega)$; standard arguments invoking Liouville's theorem imply that $H(\omega) = 0$, so that $\hat{\Psi}_Y^+(\omega,1) = B^+(\omega)C^+(\omega)$ and $\hat{\Psi}_{YY}^-(\omega,1) = C^-(\omega)/B^-(\omega)$. Thus (D 10) and (D 5) yield two representations for $A(\omega)$, each of which is the analytic continuation of the other and regular in $R^\pm$ respectively. In the limit $\epsilon\to 0$, both representations satisfy $A(\omega) \sim 3\mathrm{i}\omega^{-5}(1 + \mathrm{i}\Omega\omega)$ as $\omega\to 0$, where Ω is given by (D 8), and in this limit

$$\hat{\Psi}_Y^+(\omega,1) = \frac{\mathrm{i}}{\omega}\left[1 + 4B^+(\omega)\right] \sim \Omega, \quad \hat{\Psi}_{YY}^-(\omega,1) = -\frac{4\mathrm{i}}{\omega}\frac{1}{B^-(\omega)} \sim -\frac{4\mathrm{i}}{\omega}(1 + \mathrm{i}\Omega\omega). \tag{D 11}$$

By considering the limit $|\omega| \to \infty$, with $\mathrm{Im}\,\omega > 0$, it follows from (D 3), (D 4), (D 7), (D 11) that $\Lambda = (8/\pi)^{1/2}$ in agreement with Kim & Chung (1984). Also, from (3.4) and (D 11)

$$\Upsilon = \lim_{\epsilon\to 0}\lim_{X\to-\infty}\left[\int_X^0 \left(\Psi_{YY}(X,1) - 4\mathrm{e}^{\epsilon X}\right)\,\mathrm{d}X\right] = \lim_{\epsilon\to 0}\lim_{\omega\to 0}\left[\hat{\Psi}^-_{YY}(\omega,1) - \frac{4}{\epsilon + \mathrm{i}\omega}\right] = 4\Omega,$$

where $\omega \to 0$ with $\mathrm{Im}\,\omega < 0$. Likewise, using (3.5) one finds that

$$-\Theta = \lim_{\omega\to 0}\left[\hat{\Psi}_{YYY}(\omega,0) + \frac{12\mathrm{i}}{\omega}\right] = 24\mathrm{i}B^+_\omega(0) = 6\Omega.$$

REFERENCES

Agrawal, M. L. & Neuman, R. D. 1988 Surface diffusion in monomolecular films. II. Experiment and theory. *J. Colloid Interface Sci.* **121**, 366–380.

Badr, H., Dennis, S. C. R., Bates, S. & Smith, F. T. 1985 Numerical and asymptotic solutions for merging flow through a channel with an upstream splitter plate. *J. Fluid Mech.* **156**, 63–81.

Bel Fdhila, R. & Duineveld, P. C. 1996 The effect of surfactant on the rise of a spherical bubble at high Reynolds and Péclet numbers. *Phys. Fluids* **8**, 310–321.

Bois, A. G. & Panaiotov, I. 1995 Nonsteady effects due to a small surface pressure perturbation in an elastic insoluble monolayer. *J. Colloid Interface Sci.* **170**, 25–30.

Borgas, M. S. & Grotberg, J. B. 1988 Monolayer flow on a thin film. *J. Fluid Mech.* **193**, 151–170.

Carpenter, B. & Homsy, G. M. 1985 The effect of surface contamination on thermocapillary flow in a two-dimensional slot. Part 2. Partially contaminated interfaces. *J. Fluid Mech.* **155**, 429–439.

Carrier, G. F. & Lin, C. C. 1948 On the nature of the boundary layer near the leading edge of a flat plate. *Q. Appl. Maths* **6**, 63–68.

Cuenot, B., Magnaudet, J. & Spennato, B. 1997 The effects of slightly soluble surfactants on the flow around a spherical bubble. *J. Fluid Mech.* **339**, 25–53.

Davis, A. M. J. & Abrahams, I. D. 1996 Asymmetric channel divider and the Stokes entry problem. *Bull. Am. Phys. Soc.* **41**(9), abstract EN1.

Dimitrov, D. S., Panaiotov, I., Richmond, P. & Ter-Minassian-Saraga, L. 1978 Dynamics of insoluble monolayers. I. Dilatational or elastic modulus, friction coefficient, and Marangoni effect for dipalmitoyl lecithin monolayers. *J. Colloid Interface Sci.* **65**, 483–494.

Dussan V., E. B. 1979 On the spreading of liquid on solid surfaces: static and dynamic contact lines. *Ann. Rev. Fluid Mech.* **65**, 71–95.

Espinosa, F. F., Shapiro, A. H., Fredberg, J. J. & Kamm, R. D. 1993 Spreading of a small surfactant bolus on a thin film lining an airway. *J. Appl. Physiol.* **75**, 2028–2039.

Floryan, J. M. & Czechowski, L. 1995 On the numerical treatment of corner singularity in the vorticity field. *J. Comput. Phys.* **118**, 222–228.

Foote, R. M. L. & Buchwald, V. T. 1985 An exact solution for the stress intensity factor for a double cantilever beam. *Intl J. Fracture* **29**, 125–134.

Gaver, D. P. III & Grotberg, J. B. 1990 The dynamics of localized surfactant on a thin film. *J. Fluid Mech.* **213**, 127–148.

Gaver, D. P. III & Grotberg, J. B. 1992 Droplet spreading on a thin viscous film. *J. Fluid Mech.* **235**, 399–414.

Graebel, W. P. 1965 Slow viscous shear flow past a plate in a channel. *Phys. Fluids* **8**, 1929–1935.

Grotberg, J. B. 1994 Pulmonary flow and transport phenomena. *Ann. Rev. Fluid Mech.* **26**, 529–571.

Grotberg, J. B. & Gaver, D. P. III 1996 A synopsis of surfactant spreading research. *J. Colloid Interface Sci.* **178**, 377–378.

Grotberg, J. B., Halpern, D. & Jensen, O. E. 1995 The interaction of exogenous and endogenous surfactant: spreading-rate effects. *J. Appl. Physiol.* **78**, 750–756.

Grundy, R. E. & McLaughlin, R. 1982 Eigenvalues of the Barenblatt-Pattle similarity solution in nonlinear diffusion. *Proc. R. Soc. Lond.* A **383**, 89–100.

HALPERN, D. & GAVER, D. P. III 1994 Boundary-element analysis of the time-dependent motion of a semi-infinite bubble in a channel. *J. Comput. Phys.* **115**, 366–375.

HARPER, J. F. 1992 The leading edge of an oil slick, soap film, or bubble stagnant cap in Stokes flow. *J. Fluid Mech.* **237**, 23–32.

HE, S. & KETTERSON, J. B. 1995 Surfactant-driven spreading of a liquid on a vertical surface. *Phys. Fluids* **7**, 2640–2647.

JENSEN, O. E. 1994 Self-similar, surfactant-driven flows. *Phys. Fluids* **6**, 1084–1094.

JENSEN, O. E. 1995 The spreading of insoluble surfactant at the free surface of a deep fluid layer. *J. Fluid Mech.* **293**, 349–378.

JENSEN, O. E. 1998 The stress singularity in surfactant-driven thin-film flows. Part 2. Inertial effects. *J. Fluid Mech.* **372**, 301–322.

JENSEN, O. E. & GROTBERG, J. B. 1992 Insoluble surfactant spreading on a thin viscous film: shock evolution and film rupture. *J. Fluid Mech.* **240**, 259–288.

JENSEN, O. E. & GROTBERG, J. B. 1993 The spreading of heat or soluble surfactant along a thin liquid film. *Phys. Fluids* A **5**, 58–68.

JENSEN, O. E., HALPERN, D. & GROTBERG, J. B. 1994 Transport of a passive solute by surfactant-driven flows. *Chem. Engng Sci.* **49**, 1107–1117.

KHESHGI, H. S. & SCRIVEN, L. E. 1991 Dewetting: nucleation and growth of dry regions. *Chem. Engng Sci.* **46**, 519–526.

KIM, M.-U. & CHUNG, M. K. 1984 Two-dimensional slow viscous flow past a plate midway between an infinite channel. *J. Phys. Soc. Japan* **53**, 156–166.

KING, J. R. & PLEASE, C. P. 1986 Diffusion of dopant in crystalline silicon: an asymptotic analysis. *IMA J. Appl. Maths* **37**, 185–197.

LA DUE, J., MULLER, M. R., SWANGLER, M. 1996 Cratering phenomena on aircraft anti-icing films. *J. Aircraft* **33**, 131–138.

MALVANO, R. & VATTA, F. 1998 Lubricated plane slider bearing: solution of the inlet problem with upstream free surface. *J. Fluid Mech.* **359**, 281–297.

MICHAEL, D. H. 1958 The separation of a viscous liquid at a straight edge. *Mathematika* **5**, 82–84.

MOFFATT, H. K. 1964 Viscous and resistive eddies near a sharp corner. *J. Fluid Mech.* **18**, 1–18.

NOBLE, B. 1958 *Methods Based on the Wiener-Hopf Technique*. Chelsea Press, New York.

O'BRIEN, S. P. G. M. 1993 On Marangoni drying: nonlinear kinematics waves in a thin film. *J. Fluid Mech.* **254**, 649–670.

PARK, C.-W. 1992 Influence of soluble surfactants on the motion of a finite bubble in a capillary tube. *Phys. Fluids* A **4**, 2335–2347.

PATTLE, R. E. 1959 Diffusion from an instantaneous point source with a concentration-dependent coefficient. *Q. J. Mech. Appl. Maths* **12**, 407–409.

PAWAR, Y. & STEBE, K. J. 1996 Marangoni effects on drop deformation in an extensional flow: the role of surfactant physical chemistry. I. Insoluble surfactants. *Phys. Fluids* **8**, 1738–1751.

PIMPUTKAR, S. M. & OSTRACH, S. 1980 Transient thermocapillary flow in thin liquid layers. *Phys. Fluids* **23**, 1281–1285.

PORTER, D. & DORE, B. D. 1974 The effect of a semi-contaminated free surface on mass transport. *Proc. Camb. Phil. Soc.* **75**, 283–294.

RICHARDSON, S. 1970 A 'stick-slip' problem related to the motion of a free jet at low Reynolds numbers. *Proc. Camb. Phil. Soc.* **67**, 477–489.

SALAMON, T. R., BORNSIDE, D. E., ARMSTRONG, R. C. & BROWN, R. A. 1995 The role of surface tension in the dominant balance in the die swell singularity. *Phys. Fluids* **7**, 2328–2344.

SCHULTZ, W. W. & GERVASIO, C. 1990 A study of the singularity in the die-swell problem. *Q. J. Mech. Appl. Maths* **43**, 407–425.

SEN, A. K. & DAVIS, S. H. 1982 Steady thermocapillary convection in two-dimensional slots. *J. Fluid Mech.* **121**, 163–186.

SMITH-WHITE, W. B. & BUCHWALD, V. T. 1964 A generalization of $z!$ *J. Australian Math. Soc.* **4**, 327–341.

TANNER, R. I. & HUANG, X. 1993 Stress singularities in non-Newtonian stick–slip and edge flows. *J. Non-Newtonian Fluid Mech.* **50**, 135–160.

TAYLER, A. B. 1973 Singularities at flow separation points. *Q. J. Mech. Appl. Maths* **26**, 153–172.

Thess, A., Spirn, D. & Jüttner, B. 1997 A two-dimensional model for slow convection at infinite Marangoni number. *J. Fluid Mech.* **331**, 283–312.

Trogdon, S. A. & Joseph, D. D. 1980 The stick-slip problem for a round jet: I. Large surface tension. *Rheol. Acta* **19**, 404–420.

Trogdon, S. A. & Joseph, D. D. 1981 The stick-slip problem for a round jet: II. Small surface tension. *Rheol. Acta* **20**, 1–13.